©ESO 2019

Anomalous peculiar motions of high-mass young stars in the Scutum spiral arm

K. Immer[1], J. Li[2], L. H. Quiroga-Nuñez[3,1], M. J. Reid[4], B. Zhang[5], L. Moscadelli[6], and K. L. J. Rygl[7]

[1] Joint Institute for VLBI ERIC, Oude Hoogeveensedijk 4, 7991 PD Dwingeloo, The Netherlands; email: `immer@jive.eu`
[2] Purple Mountain Observatory CAS, No.8 Yuanhua Road, Qixia District, Nanjing 210034, The People's Republic of China
[3] Leiden Observatory, Leiden University, Niels Bohrweg 2, NL-2333CA, Leiden, The Netherlands
[4] Center for Astrophysics | Harvard & Smithsonian, 60 Garden Street, Cambridge, MA 02138, USA
[5] Shanghai Astronomical Observatory, 80 Nandan Road, Shanghai 200030, China
[6] Instituto Nationale di Astrofisica, Osservatorio Astrofisico di Arcetri, Largo Enrico Fermi 5, I-50125 Firenze, Italia
[7] Italian ALMA Regional Centre, INAF-Istituto di Radioastronomia, Via P. Gobetti 101, 40129 Bologna, Italy

ABSTRACT

We present trigonometric parallax and proper motion measurements toward 22 GHz water and 6.7 GHz methanol masers in 16 high-mass star-forming regions. These sources are all located in the Scutum spiral arm of the Milky Way. The observations were conducted as part of the Bar and Spiral Structure Legacy (BeSSeL) survey. A combination of 14 sources from a forthcoming study and 14 sources from the literature, we now have a sample of 44 sources in the Scutum spiral arm, covering a Galactic longitude range from 0° to 33°. A group of 16 sources shows large peculiar motions of which 13 are oriented toward the inner Galaxy. A likely explanation for these high peculiar motions is the combined gravitational potential of the spiral arm and the Galactic bar.

arXiv:1911.06806v2 [astro-ph.GA] 18 Nov 2019

1. Introduction

Our Galaxy has been identified as a barred spiral galaxy (de Vaucouleurs 1970). However, due to our position in the Milky Way, many details concerning the exact shape of our Galaxy are still under debate (e.g., the number and position of the spiral arms, the rotation curve or the shape of the bar; Reid & Honma 2014). To resolve some of these issues, reliable distance measurements to objects in the spiral arms are necessary. The high astrometric accuracies provided by very long baseline interferometry (VLBI) allow the determination of trigonometric parallaxes to maser sources in high-mass star-forming regions all over the Galaxy (Honma et al. 2012; Reid & Honma 2014; Sanna et al. 2017). Since these regions are located within the spiral arms (e.g., Elmegreen 2011), this approach allows a precise mapping of the spiral structure of the Milky Way. This technique also provides proper motion measurements for the maser sources; thus, we determine the positions of the sources in 6D space (coordinates, distance, line-of-sight velocity, and proper motion).

In recent years, the Bar and Spiral Structure Legacy (BeSSeL[1], Brunthaler et al. 2011) survey, an NRAO[2] Very Long Baseline Array (VLBA) key science project, has measured the parallaxes and proper motion of over 100 star-forming regions across the Milky Way (e.g., Reid et al. 2014; Sato et al. 2014; Wu et al. 2014; Choi et al. 2014; Sanna et al. 2014; Hachisuka et al. 2015). In this paper we discuss BeSSeL survey results for maser sources in the Scutum (also called Scutum-Centaurus or Scutum-Crux) spiral arm.

The Scutum spiral arm is located in the inner Galaxy (from the Sun's point of view), between the Sagittarius and the Norma arms. The Scutum arm was identified as strong condensations in neutral hydrogen and CO observations (Shane 1972; Cohen et al. 1980; Dame et al. 1986, 2001) in longitude-velocity plots. Sato et al. (2014) presented the first BeSSeL survey results for 16 Scutum arm sources, discussing the location of the arm and its pitch angle, as well as the peculiar motions of the sources. We now have a larger sample of sources in the Scutum arm and can thus improve on pinpointing the spiral arm location, and we can study the kinematics in the arm.

We present new distances and kinematic information for 16 high-mass star-forming regions in the Scutum arm. Another 14 sources of this arm will be published in Li et al. (in prep.). While Li et al. discuss the pitch angle of the Scutum spiral arm, we focus on the kinematics in the arm, especially a group of sources with anomalously large peculiar motion. In addition to the sources from Li et al., we also included 14 sources from the literature (Bartkiewicz et al. 2008; Xu et al. 2011; Immer et al. 2013; Sato et al. 2014; Zhang et al. 2014) in our peculiar motion analysis. We first describe the observations (Sect. 2) and then present our results (Sect. 3), including the parallax and proper motion fits for the 16 sources, the association of the sources with the Scutum spiral arm, and the measured peculiar motion of all 44 sources. In Sect. 4, we discuss the anomalously large peculiar motions of 16 sources and explore their possible origins.

2. Observations and data reduction

We conducted multi-epoch phase-referenced observations with the VLBA of 13 6.7 GHz methanol masers and three 22 GHz water masers, located within high-mass star-forming regions.

---

[1] `http://bessel.vlbi-astrometry.org/`
[2] The National Radio Astronomy Observatory is a facility of the National Science Foundation operated under cooperative agreement by Associated Universities, Inc.

The coordinates of the sources, program codes, and observing epochs are given in Table A.1. For the methanol masers, four epochs spread over one year are scheduled to optimally sample the extent of the Earth's orbit around the Sun as viewed by the targets (corresponding to the peaks of the sinusoidal parallax signature) in right ascension and to minimize the correlation between the parallax and proper motion contributions (Xu et al. 2006; Menten et al. 2007). Since water maser spots can be shorter-lived than one year (Tarter & Welch 1986), two additional epochs are observed at 22 GHz. Compact background sources, used as position references for the maser targets, were selected from the ICRF2 catalog (Fey et al. 2015) and a dedicated VLBA survey of extragalactic sources (Immer et al. 2011). The background quasars that were observed with each target are listed in Table A.1.

The general observation setup and the data reduction procedures are detailed in Reid et al. (2009). Except for G028.86+00.06, four adjacent frequency bands with 16 MHz width (8 MHz for G028.86+00.06) were observed in right and left circular polarization. The maser emission was centered in the third (second for G028.86+00.06) frequency band, at the LSR velocity of the target (see Table A.1). The data were correlated in two steps, one for the continuum data and one for the maser line data. For the maser line data, the frequency resolution was 8 kHz (BR198), 16 kHz (BR149), or 31.25 kHz (G028.86+00.06). This corresponds to a velocity resolution of 0.36 km s^{-1} and 0.72 km s^{-1}, respectively, for the 6.7 GHz masers and 0.11 km s^{-1} for the 22 GHz masers (BR198; 0.42 km s^{-1} for the water maser G028.86+00.06), assuming rest frequencies of 6668.56 MHz for the CH$_3$OH(5_1-6_0) and 22235.0 MHz for the H$_2$O(6_{16}-5_{23}) maser transitions. The spectra of the masers are shown in Fig. B.1.

The calibration and analysis of the BeSSeL survey data was conducted using ParselTongue (Kettenis et al. 2006) scripts for the NRAO Astronomical Image Processing System (AIPS, Greisen 2003). The different calibration steps are described in Reid et al. (2009). After calibration, the background sources and the target masers were imaged with the AIPS task IMAGR. Then their relative positions were determined by fitting the brightness distribution of the feature with an elliptical Gaussian model, using the AIPS task JMFIT.

Different numbers of maser spots were selected for parallax fitting in each target maser (see Table C.1). The positional differences between the maser spots and each of the quasars were calculated and then modeled with a combination of a sinusoidal parallax signature and linear proper motion in each coordinate. Systematic uncertainties (typically from unmodeled atmospheric and ionospheric delays) are normally much larger than the formal position uncertainties from the Gaussian fitting (Menten et al. 2007), leading to high reduced χ^2 in the parallax and proper motion modeling. To account for these uncertainties, we added additional error values in quadrature to the formal position uncertainties on both coordinates and adjusted them until the reduced χ^2 for each coordinate was near unity (see Reid et al. 2009).

If several maser spots are combined in the final parallax fit, we increased the formal uncertainty on the parallax fit by a factor of $\sqrt{N_{Spot}}$, where N$_{Spot}$ is the number of combined maser spots. We make the conservative assumption that position variations of the maser spots are 100% correlated, which can be caused by small changes in the background sources or residual unmodeled atmospheric delays affecting equally all maser spots per epoch. Data from the different background quasars are assumed to be uncorrelated.

In the combined parallax fitting, we allowed for different proper motion values for different maser spots due to possible internal motions in the star-forming regions. However, if the position differences of a maser spot were measured to more than one background source, then the proper motion of this maser was constrained to be the same for all the background sources used in the parallax fitting of this spot since we assume that the background sources do not have any measurable proper motion.

For the 6.7 GHz masers, in sources where we had background sources on both sides of the target, we detected gradients of the parallax values on the sky for the parallaxes determined from different background sources (Reid et al. 2017). This is not an issue for the 22 GHz masers, which indicates unmodeled ionospheric delays as the root of this problem since ionospheric dispersive delays scale with ν^{-2}, and thus residual dispersive delays are much larger at 6.7 GHz. By simultaneously fitting for parallax parameters as well as these ionospheric effects, we improved the modeling of the position offset data (maser spot minus quasar position), yielding a more reliable parallax estimate. More details are given in Reid et al. (2017) and Zhang et al. (2019).

3. Results

3.1. Parallax fits

The parallax and proper motion results are listed in Table 1. The parallax fits are shown in Figs. 1 and C.1. The internal motion of eight maser sources are plotted in Fig. D.1 in the online Appendix.

3.2. Spiral arm association

The masers of the BeSSeL survey are assigned to the different spiral arms by associating the high-mass star-forming regions, which harbor the masers, with molecular clouds in the CO Galactic plane survey of Dame et al. (2001) and then associating the clouds with a spiral structure in l-v space. These assignments can be tested by locating the masers in plan view plots of the Milky Way, where they tend to trace out continuous arcs that can be identified as portions of spiral arms. Our sources are selected to be part of the Scutum spiral arm (see Li et al., in prep.).

3.3. Peculiar motion

In the peculiar motion analysis we included four additional 12 GHz methanol masers and ten 22 GHz water masers from the literature (see Col. 7 of Table 2), as well as 14 maser sources that will be published and discussed in more detail in Li et al. (in prep.), yielding a total of 44 maser sources tracing the Scutum spiral arm.

Transforming the measured three-dimensional motions of the 44 Scutum arm masers (proper motion plus line-of-sight velocity) to a reference frame that rotates with the Galactic disk, we yield their peculiar motion (U$_s$, V$_s$, W$_s$), where U$_s$ increases toward the Galactic center, V$_s$ in the direction of Galactic rotation, and W$_s$ toward the north Galactic pole. As the rotation model, we used a Universal rotation curve (Persic et al. 1996) with the *A5* fit values of Reid et al. (2019, Table 3) and a distance to the Galactic center of 8.15 kpc, giving a rotation speed of 236 km s^{-1}. The motion of the Sun in this reference frame is U$_\odot$ = 10.6 km s^{-1}, V$_\odot$ = 10.7 km s^{-1}, and W$_\odot$ = 7.6 km s^{-1}. The calculated peculiar motion components of the Scutum arm

Table 1: Parallax and proper motion results[a].

Source	π	Distance	μ_x[b]	μ_y[b]	v_{lsr}
	[mas]	[kpc]	[mas yr^{-1}]	[mas yr^{-1}]	[km s^{-1}]
G023.25−00.24	0.169 ± 0.051	$5.92 ^{+2.56}_{-1.37}$	-1.72 ± 0.14	-4.06 ± 0.20	63 ± 3
G028.14−00.00	0.158 ± 0.023	$6.33 ^{+1.08}_{-0.80}$	-2.11 ± 0.03	-4.85 ± 0.03	100 ± 5
G028.86+00.06*	0.201 ± 0.019	$4.98 ^{+0.52}_{-0.43}$	-3.19 ± 0.05	-5.72 ± 0.24	100 ± 10
G029.86−00.04*c	0.221 ± 0.015	$4.52 ^{+0.33}_{-0.28}$	-2.30 ± 0.01	-5.33 ± 0.02	100 ± 4
G029.95−00.01*d	0.222 ± 0.018	$4.50 ^{+0.40}_{-0.33}$	-2.32 ± 0.02	-5.38 ± 0.02	99 ± 5
G029.98+00.10*	0.156 ± 0.010	$6.41 ^{+0.44}_{-0.39}$	-1.39 ± 0.03	-3.49 ± 0.20	109 ± 10
G030.22−00.18	0.284 ± 0.032	$3.52 ^{+0.45}_{-0.36}$	-0.87 ± 0.08	-4.70 ± 0.15	113 ± 3
G030.41−00.23*	0.253 ± 0.021	$3.95 ^{+0.36}_{-0.30}$	-1.98 ± 0.09	-4.07 ± 0.12	103 ± 3
G030.70−00.06*	0.153 ± 0.020	$6.54 ^{+0.98}_{-0.76}$	-2.33 ± 0.08	-5.13 ± 0.09	89 ± 3
G030.74−00.04*	0.326 ± 0.055	$3.07 ^{+0.62}_{-0.44}$	-2.38 ± 0.16	-4.46 ± 0.16	88 ± 3
G030.78+00.20	0.140 ± 0.032	$7.14 ^{+2.12}_{-1.33}$	-1.85 ± 0.05	-3.91 ± 0.12	82 ± 5
G030.81−00.05	0.321 ± 0.037	$3.12 ^{+0.41}_{-0.32}$	-2.34 ± 0.08	-5.66 ± 0.16	105 ± 5
G030.97−00.14	0.294 ± 0.022	$3.40 ^{+0.28}_{-0.24}$	-2.14 ± 0.02	-3.82 ± 0.13	77 ± 3
G031.41+00.30*	0.267 ± 0.029	$3.75 ^{+0.46}_{-0.37}$	-1.38 ± 0.07	-5.70 ± 0.08	97 ± 15
G032.04+00.05e	0.195 ± 0.008	$5.13 ^{+0.22}_{-0.20}$	-1.71 ± 0.11	-4.51 ± 0.13	98 ± 5
G033.09−00.07	0.134 ± 0.016	$7.46 ^{+1.01}_{-0.80}$	-2.46 ± 0.02	-5.32 ± 0.03	100 ± 5

Notes.
[a] Additional 14 Scutum arm sources will be published in Li et al. (in prep.).
[b] The proper motion values in the table correspond to the proper motion of the maser spot underlined in Figs. 1 and C.1, except for sources marked with a star for which the proper motion corresponds to the proper motion estimate of the central object (see online Appendix D for more details).
[c] Weighted combined result of this work for the 6.7 GHz methanol maser (π=(0.307±0.024) mas, $\mu_x = (-2.36\pm0.07)$ mas yr^{-1}, $\mu_y = (-5.60\pm0.15)$ mas yr^{-1}, v_{lsr}=(101±3) km s^{-1}) and the results of Zhang et al. (2014) for the 12 GHz methanol maser (π=(0.161±0.020) mas, $\mu_x = (-2.30\pm0.01)$ mas yr^{-1}, $\mu_y = (-5.32\pm0.02)$ mas yr^{-1}, v_{lsr}=(100±3) km s^{-1}).
[d] Weighted combined result of this work for the 6.7 GHz methanol maser (π=(0.352±0.040) mas, $\mu_x = (-2.38\pm0.12)$ mas yr^{-1}, $\mu_y = (-5.37\pm0.23)$ mas yr^{-1}, v_{lsr}=(99±5) km s^{-1}) and results of Zhang et al. (2014) for the 12 GHz methanol maser (π=(0.190±0.020) mas, $\mu_x = (-2.32\pm0.02)$ mas yr^{-1}, $\mu_y = (-5.38\pm0.02)$ mas yr^{-1}, v_{lsr}=(98±3) km s^{-1}).
[e] Weighted combined result of this work for the 6.7 GHz methanol maser (π=(0.299±0.053) mas, $\mu_x = (-1.67\pm0.11)$ mas yr^{-1}, $\mu_y = (-4.47\pm0.14)$ mas yr^{-1}, v_{lsr}=(98±5) km s^{-1}) and results of Sato et al. (2014) for the 12 GHz methanol maser (π=(0.193±0.008) mas, $\mu_x = (-2.21\pm0.40)$ mas yr^{-1}, $\mu_y = (-4.80\pm0.40)$ mas yr^{-1}, v_{lsr}=(97±5) km s^{-1}).

sources are listed in Table 2. The medians of the uncertainties on the U_S, V_S, and W_S components are 10 km s^{-1}, 5 km s^{-1}, and 3 km s^{-1}, respectively. Figure 2 shows the peculiar motion of the Scutum maser sources with uncertainties of less than 20 km s^{-1} in the plane of the Galaxy.

4. Discussion

The left panels in Fig. 3 show the distribution of the peculiar motion vector components U_S, V_S, and W_S for sources with an uncertainty on the components of less than 20 km s^{-1} (32 maser sources). For the V_S and W_S components, the mean and median of the distributions are close to zero and most of the sources have values for these two components between −20 and 20 km s^{-1}. For U_S, however, the mean and median are 15.7 and 15.3 km s^{-1}, respectively, and half of the sources have velocity magnitudes > 20 km s^{-1}, indicating that the U_S component in these sources dominates the peculiar motion. In 13 of these sources,

their motion is pointed toward the inner Galaxy. In the following section, we define the high peculiar motion sources as sources with $|U_S| > 20$ km s^{-1}. We also included G010.32−00.15 in this group since this maser shows large peculiar motions as well, but in the V_S component.

Class II methanol masers (6.7, 12 GHz) are mostly located close to the protostar, while 22 GHz water masers are often detected in the outflow regions (e.g., Hofner & Churchwell 1996; Norris et al. 1998; Minier et al. 2000; Goddi et al. 2011). Since these high peculiar motions are detected in sources with all three types of masers, it is unlikely that they are caused by internal motions in the star-forming regions due to outflows for example.

To understand if there is a fundamental difference in the characteristics of the host clouds of the high and the low peculiar motion masers, we compared the cloud masses, dust temperatures, bolometric luminosities, and H_2 column densities of our sources from the APEX Telescope Large Area Survey of the Galaxy (ATLASGAL) clump catalog of Urquhart et al. (2018)

Table 2: Peculiar motions calculated based on the Galactic parameters of Reid et al. (2019).

Source	U_s[a] [km s^{-1}]	V_s[b] [km s^{-1}]	W_s[c] [km s^{-1}]	Reference
G000.31−00.20	18 ± 3	−6 ± 6	−8 ± 6	(1)
G005.88−00.39	−3 ± 3	−13 ± 5	−11 ± 5	(2)
G009.21−00.20	21 ± 38	−5 ± 41	4 ± 7	(1)
G010.32−00.15	3 ± 5	−72 ± 5	16 ± 1	(1)
G010.34−00.14	−5 ± 5	−20 ± 4	8 ± 2	(1)
G011.10−00.11	−7 ± 6	−9 ± 6	−7 ± 5	(1)
G011.91−00.61	3 ± 8	9 ± 6	−12 ± 5	(2)
G012.68−00.18	41 ± 10	−8 ± 5	2 ± 3	(3)
G012.81−00.19	5 ± 7	4 ± 2	8 ± 2	(3)
G012.88+00.48	12 ± 7	−9 ± 3	−9 ± 2	Combined: (3), (4)
G012.90−00.24	16 ± 10	−6 ± 5	−8 ± 2	(3)
G012.90−00.26	17 ± 5	−6 ± 2	−1 ± 1	(3)
G013.87+00.28	8 ± 21	−8 ± 34	−10 ± 38	(2)
G016.58−00.05	21 ± 7	−8 ± 6	4 ± 6	(2)
G018.87+00.05	−7 ± 17	1 ± 6	−4 ± 6	(1)
G019.36−00.03	−3 ± 13	−16 ± 8	5 ± 6	(1)
G022.03+00.22	1 ± 15	13 ± 6	−2 ± 6	(1)
G023.25−00.24	−21 ± 43	−34 ± 31	−2 ± 7	This work
G023.65−00.12	33 ± 9	9 ± 3	5 ± 1	(5)
G024.63−00.32	−25 ± 26	−12 ± 14	−12 ± 7	(1)
G025.70+00.04	−34 ± 34	−7 ± 90	−6 ± 11	(2)
G027.36−00.16	−83 ± 48	−34 ± 36	−3 ± 8	(4)
G028.14−00.00	−7 ± 28	−6 ± 9	−3 ± 2	This work
G028.30−00.38	12 ± 13	0 ± 6	−1 ± 5	(1)
G028.39+00.08	−21 ± 10	14 ± 5	−9 ± 2	(1)
G028.83−00.25	12 ± 30	−8 ± 11	−2 ± 6	(1)
G028.86+00.06	53 ± 10	−15 ± 9	13 ± 3	This work
G029.86−00.04	43 ± 6	−4 ± 4	−1 ± 1	Combined: This work, (6)
G029.95−00.01	43 ± 7	−5 ± 4	−1 ± 1	Combined: This work, (6)
G029.98+00.10	−58 ± 17	13 ± 12	−3 ± 3	This work
G030.19−00.16	14 ± 7	20 ± 3	10 ± 1	(1)
G030.22−00.18	50 ± 10	25 ± 3	−16 ± 3	This work
G030.41−00.23	33 ± 8	17 ± 3	6 ± 2	This work
G030.70−00.06	−9 ± 20	−15 ± 5	−1 ± 3	This work
G030.74−00.04	45 ± 10	6 ± 5	9 ± 2	This work
G030.78+00.20	−67 ± 36	−26 ± 24	3 ± 3	This work
G030.81−00.05	67 ± 6	7 ± 5	0 ± 2	This work
G030.97−00.14	25 ± 5	2 ± 3	10 ± 1	This work
G031.28+00.06	23 ± 19	16 ± 4	3 ± 1	Combined: (1), (6)
G031.41+00.30	49 ± 11	2 ± 12	−16 ± 3	This work
G031.58+00.07	−4 ± 29	2 ± 10	1 ± 2	(6)
G032.04+00.05	3 ± 6	7 ± 5	−5 ± 3	Combined: This work, (2)
G033.09−00.07	−26 ± 19	−3 ± 5	−1 ± 1	This work
G033.39+00.00	−52 ± 32	−3 ± 32	−2 ± 7	(1)

Notes.
[a] Increases toward the Galactic center.
[b] Increases in the direction of Galactic rotation.
[c] Increases toward the north Galactic pole.
[ ] References. (1) Li et al. (in prep.); (2) Sato et al. (2014); (3) Immer et al. (2013); (4) Xu et al. (2011); (5) Bartkiewicz et al. (2008); (6) Zhang et al. (2014)

(Fig. E.1). The masses were corrected for our measured parallax distances. For each of the four characteristics, we conducted a Kolmogorov-Smirnov two-sample test to determine the probability that the low and high peculiar motion maser samples are drawn from the same distribution. For the cloud masses, dust temperatures, bolometric luminosities, and H_2 column densities, the test yielded p-values of 0.82, 0.26, 0.10, and 0.96, respectively. Thus, for the bolometric luminosity the probability is only 10% that the two samples come from the same distribution.

To test whether these high peculiar motion sources are unique in the Galaxy or also detected in other spiral arms, we compared the distributions of the peculiar motion components in the Scutum arm with maser sources in the Sagittarius, Local, and Perseus arms. The source information was taken from Reid et al. (2014), applying the same rotation model as for the Scutum arm sources. The distribution of the V_S and W_S components are similar. Although some sources in the other spiral arms show high velocities in the U_S component as well, their occurrence is much lower than in the Scutum spiral arm (eight sources with $|U_S| > 20$ km s^{-1} in the three arms combined compared to 16 sources in the Scutum arm). With a Kolmogorov-Smirnov two-sample test, we tested the hypothesis that the samples of the peculiar motion components of the Scutum arm and the other three spiral arms are drawn from the same distribution, yielding p-values of 0.0005, 0.02, and 0.78 for U_S, V_S, and W_S, respectively. Thus, for the U_S and V_S components, the probability is less than 5% that the Scutum arm sources are drawn from the same distribution as the other spiral arm sources. These results suggest that a local phenomenon led to the high peculiar motions of these clouds.

Gravitational attraction of the spiral arm and the Galactic bar

The formation of spiral arms in the Milky Way has been historically described via the spiral density-wave theory (for a recent review, see Lin & Shu 1964; Shu 2016). Gas within the co-rotation radius of the Galaxy (~8.5 kpc, Dias et al. 2019) moves faster than the wave itself and is accelerated radially outward when entering the interior side of the arm. Thus, this theory cannot explain the motion of our high peculiar motion sources, which is mostly directed radially inward. Including large-scale shock waves (e.g., Roberts 1969) or magnetic fields (e.g., Roberts & Yuan 1970) can give the correct sign for the peculiar motions, but their measured magnitudes might be too large to be easily explained by these models. Since we do not see many high peculiar motion sources in most spiral arms, this cannot be the full answer.

De Vaucouleurs (1970) first suggested that the Milky Way is a barred spiral galaxy. There is still a dispute about the exact shape and orientation of the bar. While some authors favor a shorter structure with a length of 2.5−3.5 kpc and a position angle with respect to the Sun–Galactic center direction of ~23° (e.g., Bissantz & Gerhard 2002; Gerhard 2002; Babusiaux & Gilmore 2005), others identified a long bar with a length of 4 kpc and a position angle of 45° (e.g., Hammersley et al. 2000; Benjamin et al. 2005; López-Corredoira et al. 2007; Anders et al. 2019). Recently, Wegg et al. (2015) identified a long bar with a half-length of 5 kpc and a position angle of 28−33°. It is not clear if these structures are fundamentally different or how they are related. Figure 4 shows the bar structures in relation to the position of the Scutum arm sources (for all three bars, a minor axis of 1.2 kpc is assumed, as in López-Corredoira et al. 2007).

López-Corredoira et al. (2007) estimated the mass of the Galactic bar as $6 \cdot 10^9$ M$_\odot$. Using this mass for the bar, we determined its gravitational potential and subsequently the terminal velocity caused solely by the bar at the distance of the high peculiar motion sources which yields 95−130 km s^{-1} for the 3.5 kpc bar, 95−165 km s^{-1} for the 4 kpc bar, and 105−145 km s^{-1} for the 5 kpc bar. Since the terminal velocity is larger than the peculiar motion of the high peculiar motion sources, the gravitational attraction of the bar is a possible explanation for these anomalous values. We do not expect the sources to move with the terminal velocity since they are not in free-fall and there is friction within the spiral arm. The Galactic models of Roberts et al. (1979) showed that large noncircular motions with radial velocities as high as 100 km s^{-1} are expected near the ends of the bar.

The peculiar motion vectors of eight high peculiar motion sources are oriented toward the tip of the short bar, hinting toward the gravitational potential of this structure being the prominent attractor. The long bar of Wegg et al. (2015) crosses the spiral arm at l~31° at a distance from the Sun of ~5 kpc where several high peculiar motion sources are located.

Although the clustering of the high peculiar motion sources in the Scutum arm hints at the potential of the bar as the dominating potential, we cannot exclude the importance of the spiral arm when in interplay with the potential of the bar. Thus, we conclude that the most likely explanation for the high peculiar motions is the combined gravitational potential of the spiral arm and the Galactic bar.

Baba et al. (2009) have shown in their N-body+hydrodynamical simulations of a barred spiral galaxy that peculiar motions of more than 25 km s^{-1} can be reproduced. However, their simulated peculiar motions appear randomly distributed over the Galaxy, and are thus not consistent with the results of the BeSSeL survey. The simulations of Khoperskov et al. (2019) show large radial velocities toward the Galactic center of 20 km s^{-1} within 0 kpc < X < 3 kpc and 3 kpc < Y < 6 kpc and a change in the direction of the peculiar motion from inward to outward near X = 4 kpc and Y = 2.5 kpc, which is consistent with most of our peculiar motions.

5. Conclusion

In this publication, we present new parallax and proper motion measurements of 16 maser sources in the Scutum spiral arm. Together with 14 maser sources from the literature and another 14 maser sources, which will be published in Li et al. (in prep.), we determined the peculiar motions in the Scutum arm. The main conclusions of our paper can be summarized as follows:

1. Sixteen sources in the Scutum spiral arm show large peculiar motions. Thirteen of these motion vectors are oriented toward the inner Galaxy.
2. These high peculiar motions are measured in all three maser types of our sources: 6.7 GHz methanol masers, 12 GHz methanol masers, and 22 GHz water masers.
3. There is a hint that the masers with high peculiar motions are hosted in clouds that are on average more luminous than those of the low peculiar motion masers.
4. This large number of sources with high peculiar motions is unique in our Galaxy; other spiral arms only harbor a small number of sources with large peculiar motions. This suggests that a local phenomenon is the cause for these larger peculiar motions.

5. The most likely explanation for the large peculiar motions is the combined gravitational attraction of the spiral arm and Galactic bar potential.

References

Anders, F., Khalatyan, A., Chiappini, C., et al. 2019, arXiv e-prints
Baba, J., Asaki, Y., Makino, J., et al. 2009, ApJ, 706, 471
Babusiaux, C. & Gilmore, G. 2005, MNRAS, 358, 1309
Bartkiewicz, A., Brunthaler, A., Szymczak, M., van Langevelde, H. J., & Reid, M. J. 2008, A&A, 490, 787
Benjamin, R. A., Churchwell, E., Babler, B. L., et al. 2005, ApJ, 630, L149
Bissantz, N. & Gerhard, O. 2002, MNRAS, 330, 591
Brunthaler, A., Reid, M. J., Menten, K. M., et al. 2011, Astronomische Nachrichten, 332, 461
Choi, Y. K., Hachisuka, K., Reid, M. J., et al. 2014, ApJ, 790, 99
Cohen, R. S., Cong, H., Dame, T. M., & Thaddeus, P. 1980, ApJ, 239, L53
Dame, T. M., Elmegreen, B. G., Cohen, R. S., & Thaddeus, P. 1986, ApJ, 305, 892
Dame, T. M., Hartmann, D., & Thaddeus, P. 2001, ApJ, 547, 792
de Vaucouleurs, G. 1970, in IAU Symposium, Vol. 38, The Spiral Structure of our Galaxy, ed. W. Becker & G. I. Kontopoulos, 18
De Vaucouleurs, G. 1970, in IAU Symposium, Vol. 38, The Spiral Structure of our Galaxy, ed. W. Becker & G. I. Kontopoulos, 18
Dias, W. S., Monteiro, H., Lépine, J. R. D., & Barros, D. A. 2019, MNRAS, 486, 5726
Elmegreen, B. G. 2011, in EAS Publications Series, Vol. 51, EAS Publications Series, ed. C. Charbonnel & T. Montmerle, 19–30
Fey, A. L., Gordon, D., Jacobs, C. S., et al. 2015, AJ, 150, 58
Gerhard, O. 2002, in Astronomical Society of the Pacific Conference Series, Vol. 273, The Dynamics, Structure & History of Galaxies: A Workshop in Honour of Professor Ken Freeman, ed. G. S. Da Costa, E. M. Sadler, & H. Jerjen, 73
Goddi, C., Moscadelli, L., & Sanna, A. 2011, A&A, 535, L8
Greisen, E. W. 2003, in Astrophysics and Space Science Library, Vol. 285, Information Handling in Astronomy - Historical Vistas, ed. A. Heck, 109
Hachisuka, K., Choi, Y. K., Reid, M. J., et al. 2015, ApJ, 800, 2
Hammersley, P. L., Garzón, F., Mahoney, T. J., López-Corredoira, M., & Torres, M. A. P. 2000, MNRAS, 317, L45
Hofner, P. & Churchwell, E. 1996, A&AS, 120, 283
Honma, M., Nagayama, T., Ando, K., et al. 2012, PASJ, 64, 136
Immer, K., Brunthaler, A., Reid, M. J., et al. 2011, ApJS, 194, 25
Immer, K., Reid, M. J., Menten, K. M., Brunthaler, A., & Dame, T. M. 2013, A&A, 553, A117
Kettenis, M., van Langevelde, H. J., Reynolds, C., & Cotton, B. 2006, in Astronomical Society of the Pacific Conference Series, Vol. 351, Astronomical Data Analysis Software and Systems XV, ed. C. Gabriel, C. Arviset, D. Ponz, & S. Enrique, 497
Khoperskov, S., Gerhard, O., Di Matteo, P., et al. 2019, arXiv e-prints
Lin, C. C. & Shu, F. H. 1964, ApJ, 140, 646
López-Corredoira, M., Cabrera-Lavers, A., Mahoney, T. J., et al. 2007, AJ, 133, 154
Menten, K. M., Reid, M. J., Forbrich, J., & Brunthaler, A. 2007, A&A, 474, 515
Minier, V., Booth, R. S., & Conway, J. E. 2000, A&A, 362, 1093
Norris, R. P., Byleveld, S. E., Diamond, P. J., et al. 1998, ApJ, 508, 275
Persic, M., Salucci, P., & Stel, F. 1996, MNRAS, 281, 27
Reid, M. J., Brunthaler, A., Menten, K. M., et al. 2017, AJ, 154, 63
Reid, M. J. & Honma, M. 2014, ARA&A, 52, 339
Reid, M. J., Menten, K. M., Brunthaler, A., et al. 2019, ApJ in press, arXiv e-prints
Reid, M. J., Menten, K. M., Brunthaler, A., et al. 2014, ApJ, 783, 130
Reid, M. J., Menten, K. M., Zheng, X. W., et al. 2009, ApJ, 700, 137
Roberts, W. W., J., Huntley, J. M., & van Albada, G. D. 1979, ApJ, 233, 67
Roberts, W. W. 1969, ApJ, 158, 123
Roberts, Jr., W. W. & Yuan, C. 1970, ApJ, 161, 887
Sanna, A., Reid, M. J., Dame, T. M., Menten, K. M., & Brunthaler, A. 2017, Science, 358, 227
Sanna, A., Reid, M. J., Menten, K. M., et al. 2014, ApJ, 781, 108
Sato, M., Wu, Y. W., Immer, K., et al. 2014, ApJ, 793, 72
Shane, W. W. 1972, A&A, 16, 118
Shu, F. H. 2016, ARA&A, 54, 667
Tarter, T. C. & Welch, W. J. 1986, ApJ, 305, 467
Urquhart, J. S., König, C., Giannetti, A., et al. 2018, MNRAS, 473, 1059
Wegg, C., Gerhard, O., & Portail, M. 2015, MNRAS, 450, 4050
Wu, Y. W., Sato, M., Reid, M. J., et al. 2014, A&A, 566, A17
Xu, Y., Moscadelli, L., Reid, M. J., et al. 2011, ApJ, 733, 25
Xu, Y., Reid, M. J., Zheng, X. W., & Menten, K. M. 2006, Science, 311, 54
Zhang, B., Moscadelli, L., Sato, M., et al. 2014, ApJ, 781, 89
Zhang, B., Reid, M. J., Zhang, L., et al. 2019, AJ, 157, 200

Appendix A: Observations

Appendix B: Maser spectra

Appendix C: Parallax measurements

Appendix D: Proper motion plots

In some of the sources we give the position and proper motion of the central object. These were determined by averaging the positions and proper motions of all maser spots with respect to a reference maser spot and then adding the proper motion of the reference maser spot. The internal motion plots of these sources show the internal motion of all maser spots with respect to the central object, which is flagged with a star symbol in the plots.

Appendix E: Cloud characteristics

Fig. 1: Parallax and proper motion data and fits for a 6.7 GHz methanol and a 22 GHz water maser. The black symbols show the average of all quasar positions for 6.7 GHz masers. In each panel, the data of different maser spots are offset for clarity. First panel: Measured position of the maser on the sky. The positions expected from the fit are shown as open circles. Second panel: East (upper part, solid lines) and north (lower part, dashed lines) position offsets vs. time. Third panel: As second panel, but with proper motion removed, showing only the parallax effect for the maser underlined in the legend.

(a) 6.7 GHz methanol maser − G023.25−00.24

(b) 22 GHz water maser − G028.86+00.06
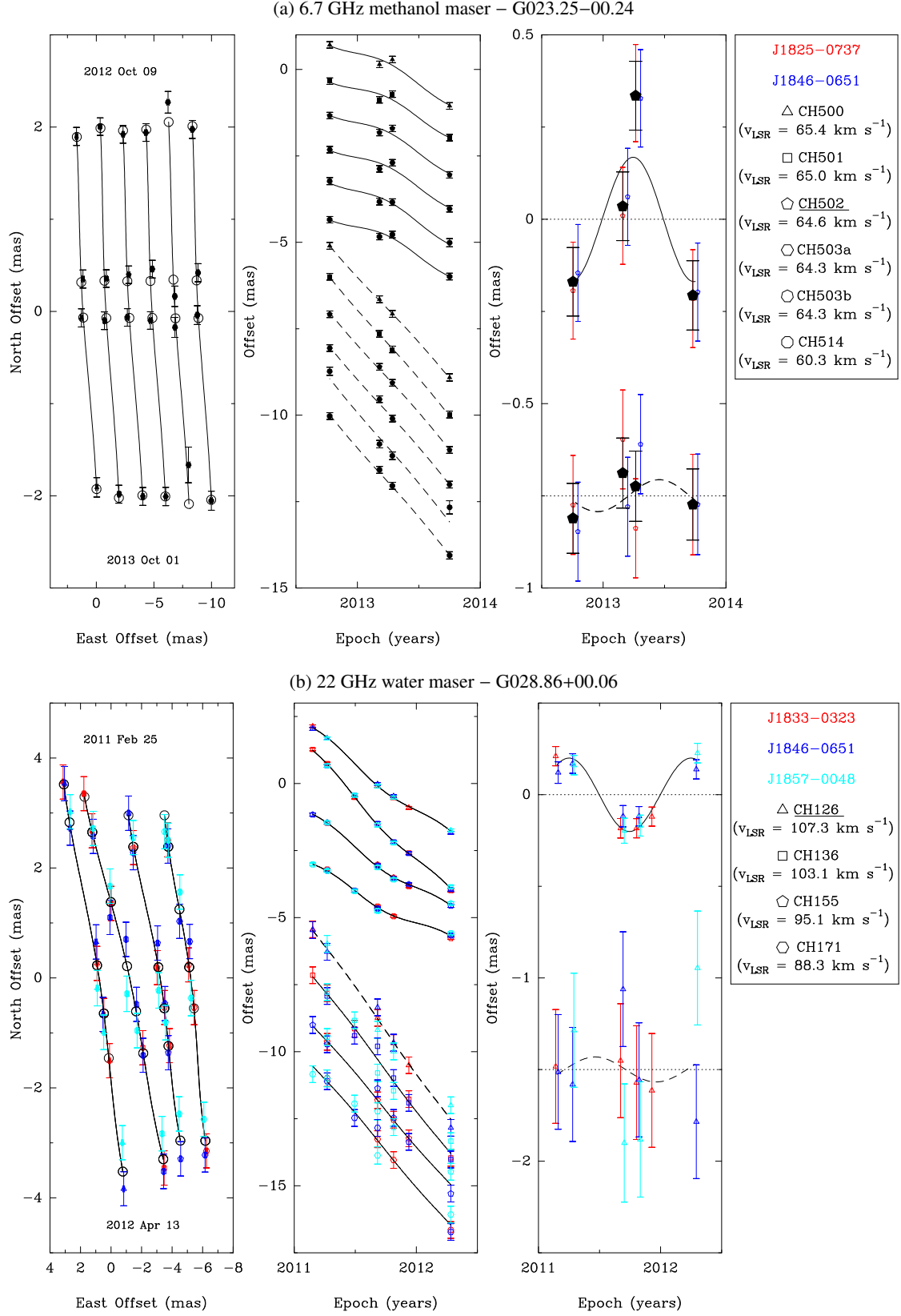
Fig. 2: Positions and peculiar motion vectors of the Scutum arm masers (blue: this paper, white: Li et al. (in prep.), gray: literature) for sources with uncertainties on the vector components of less than 20 km s^{-1}. A representative velocity vector of 20 km s^{-1} is shown in the upper right corner. The red shaded area around this vector displays the median uncertainty on the velocity vectors ($\Delta U_S = 10$ km s^{-1}, $\Delta V_S = 5$ km s^{-1}). The 22 GHz water, 6.7 GHz methanol, and 12 GHz methanol masers are indicated with circles, squares, and diamonds, respectively. The positions of the Sun and the Galactic center are indicated. The dotted lines represent the distance uncertainty on each source. The black and gray dashed lines represent the position and width of the Scutum spiral arm, as described in Sato et al. (2014).
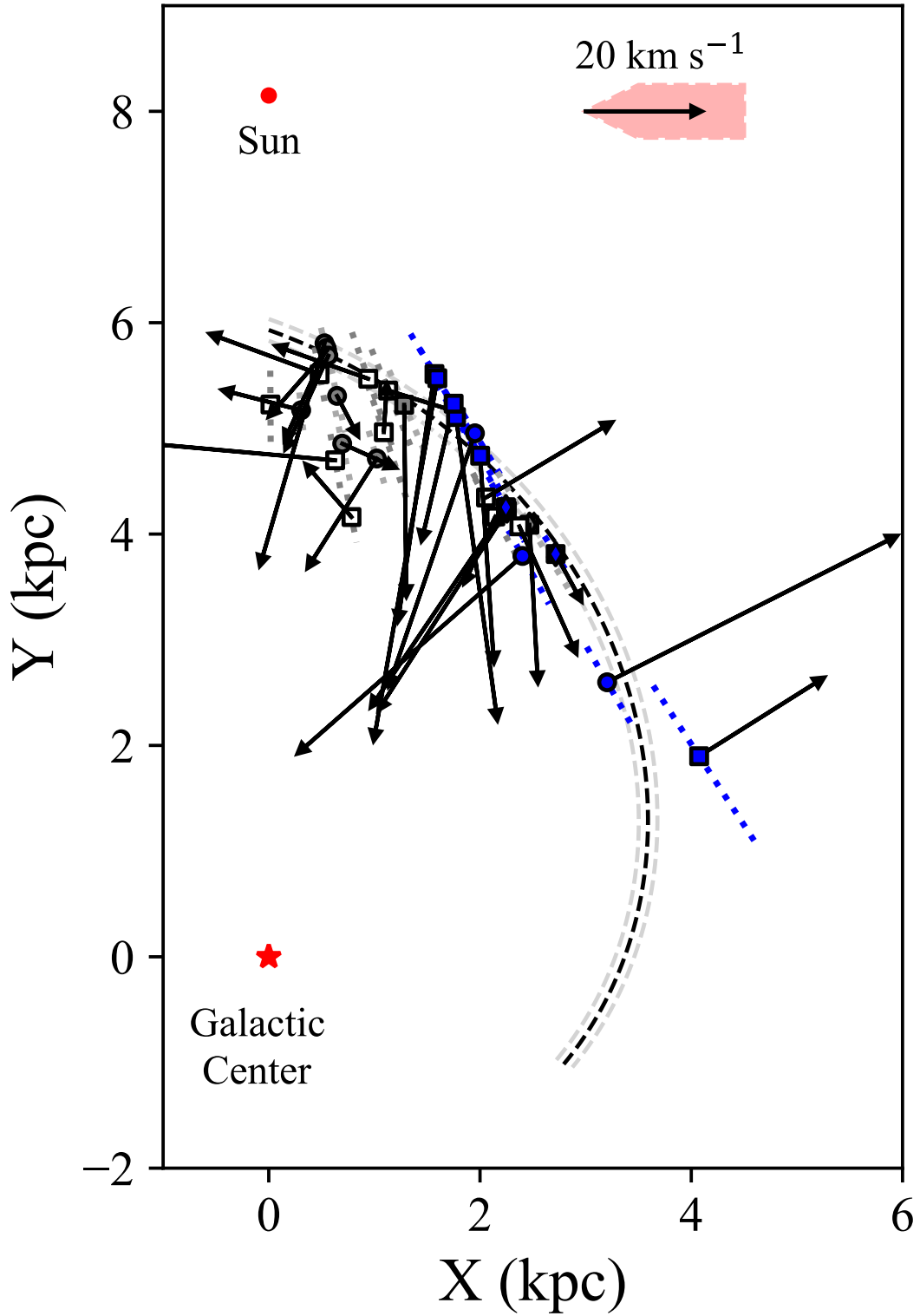
Fig. 3: Distribution of the three peculiar motion vector components U_S (upper panels), V_S (middle panels), and W_S (lower panels) for the Scutum arm sources (left) and the combined distribution of the Sagittarius, Local, and Perseus arms sources (right) with uncertainties on the peculiar motion components of less than 20 km s^{-1}.
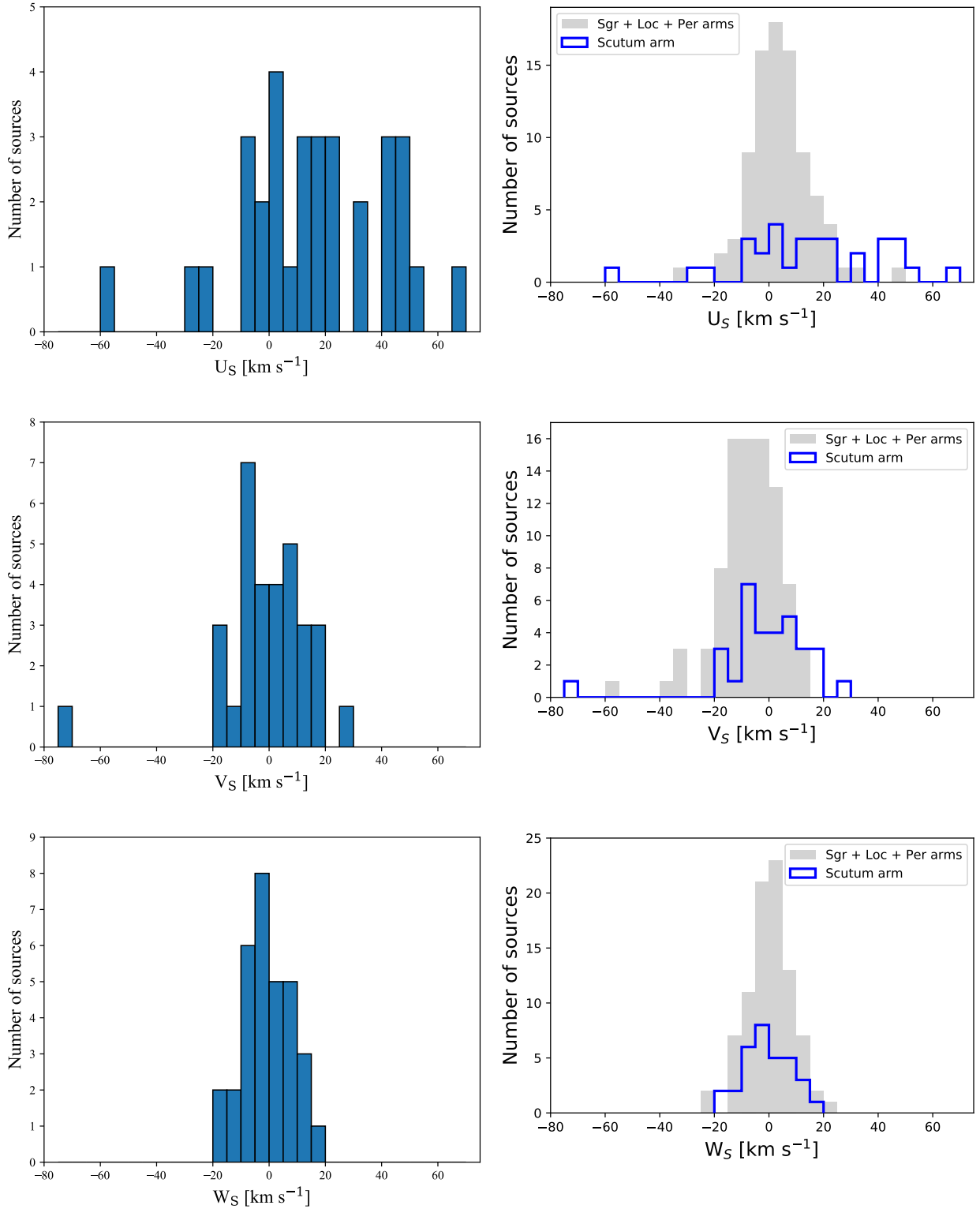
Fig. 4: Same as Fig. 2, but only the peculiar motion vectors of the high peculiar motion sources are shown (cyan). The black and gray dashed lines represent the position and width of the Scutum spiral arm as described in Sato et al. (2014). The dotted blue, dot-dashed brown, and dashed magenta lines show the locations of the bars of Bissantz & Gerhard (2002), Wegg et al. (2015), and López-Corredoira et al. (2007), respectively. A minor axis of 1.2 kpc is assumed for all three bar structures.
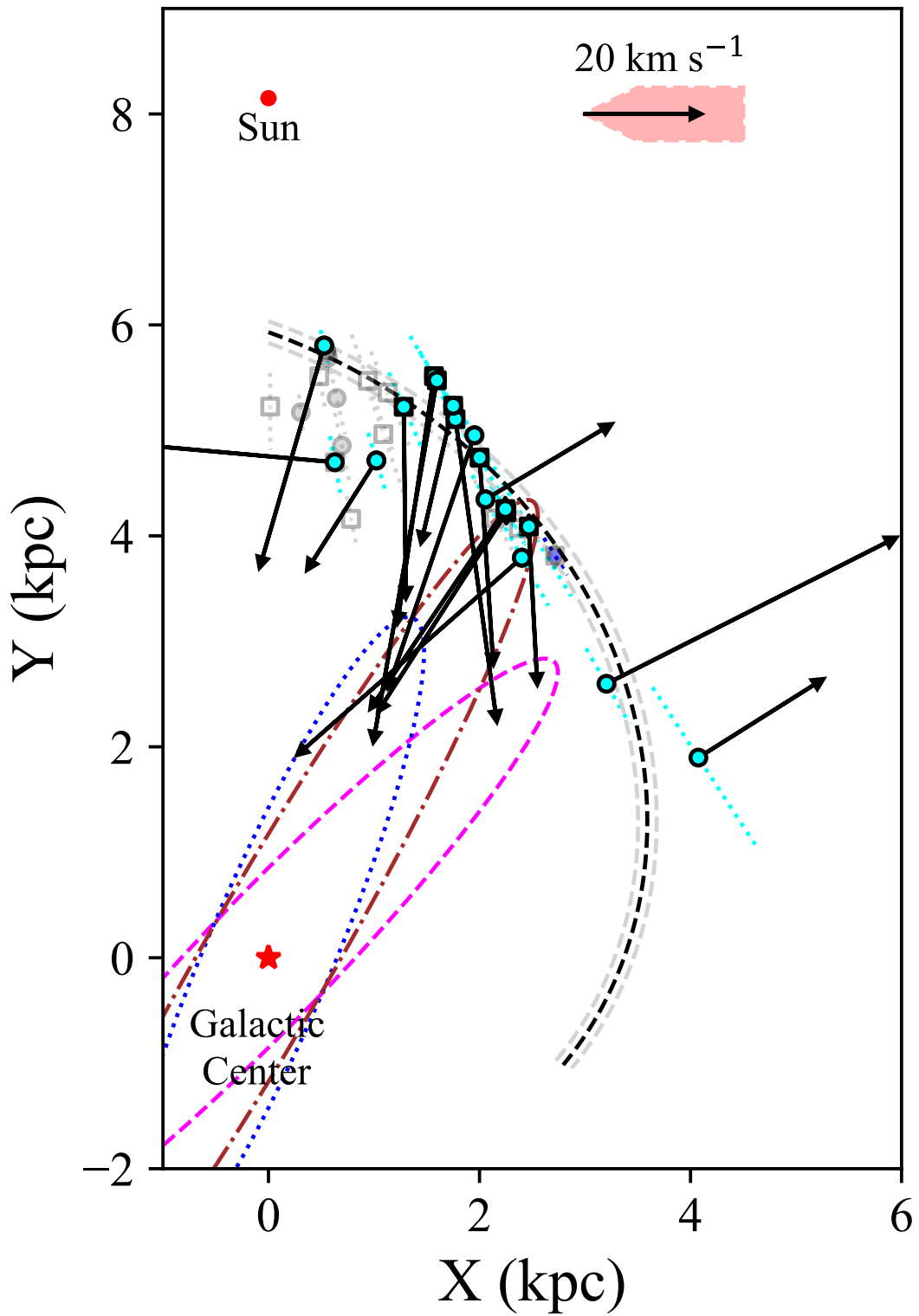
Fig. B.1: Spectra of the 16 maser sources listed in Table 1. Each spectrum is an amplitude scalar average of one-second integrations of all data on all baselines.

(a) 6.7 GHz methanol maser − G023.25−00.24 (third epoch)
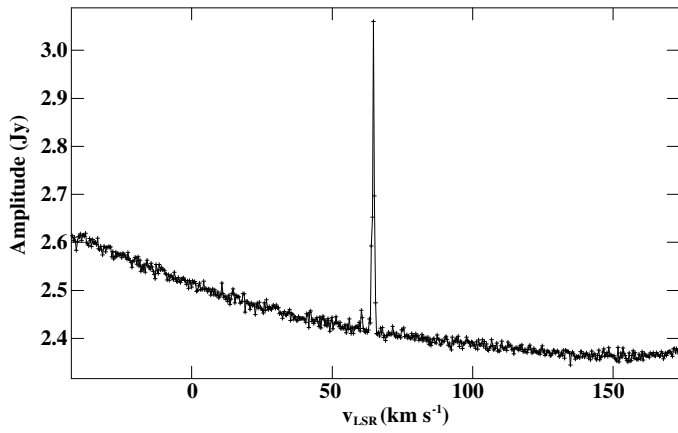
(b) 6.7 GHz methanol maser − G028.14−00.00 (first epoch)
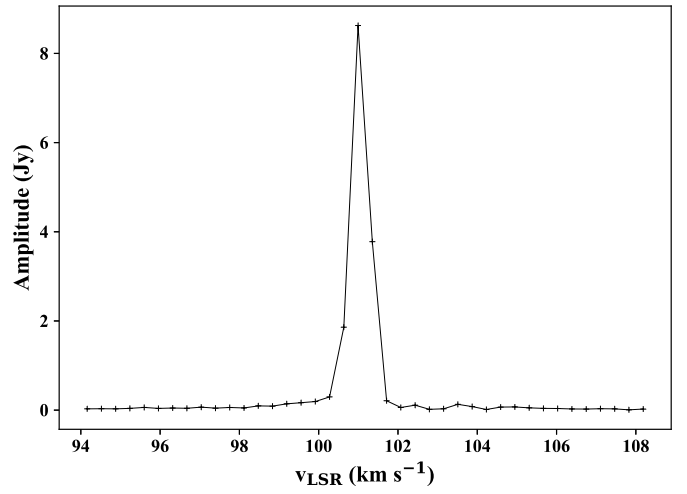
(c) 22 GHz water maser − G028.86+00.06 (second epoch)
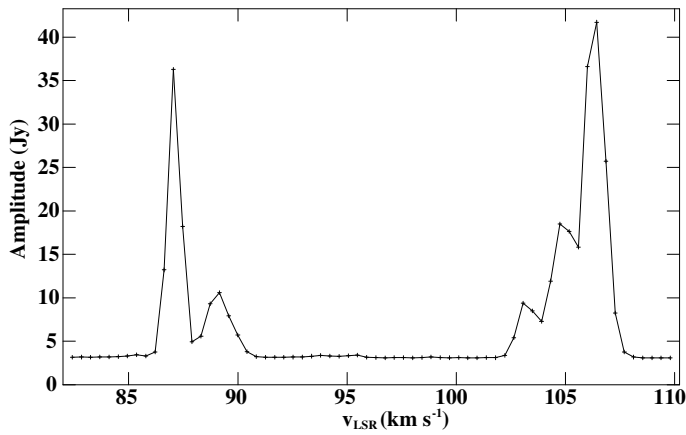
(d) 6.7 GHz methanol maser − G029.86−00.04 (second epoch)
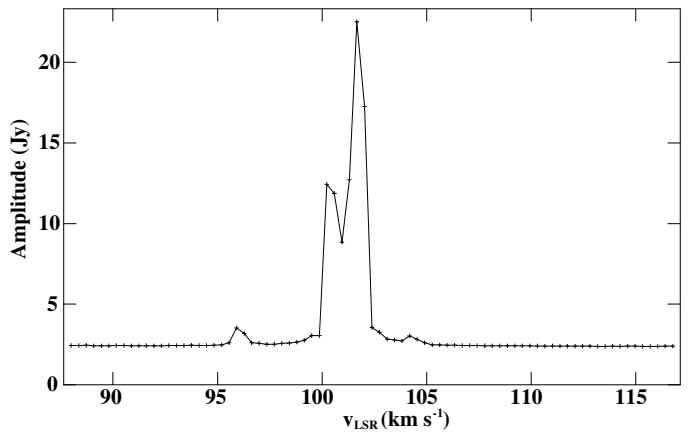
(e) 6.7 GHz methanol maser − G029.95−00.01 (second epoch)
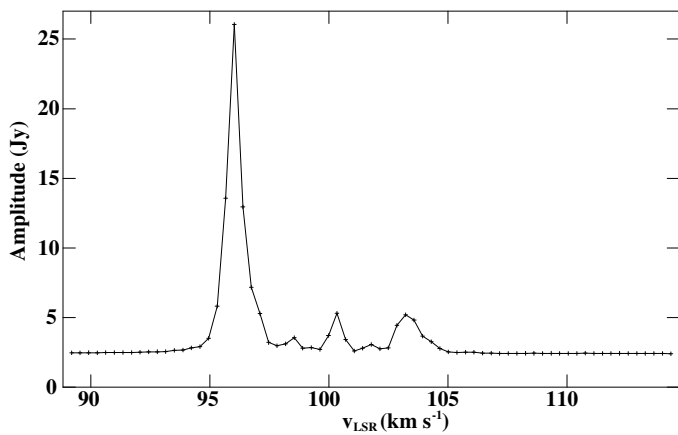
(f) 22 GHz water maser − G029.98+00.10 (second epoch)
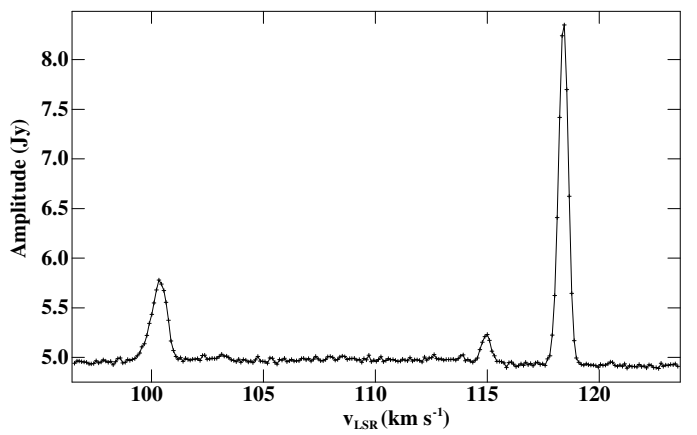
Fig. B.1: Continued.

(g) 6.7 GHz methanol maser − G030.22−00.18 (second epoch)
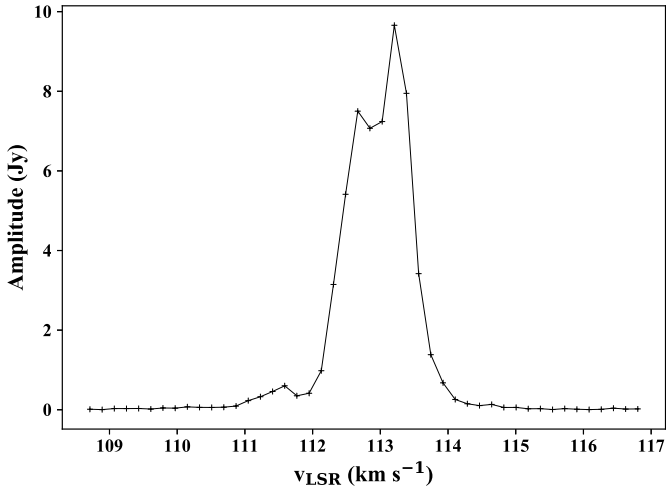
(h) 6.7 GHz methanol maser − G030.41−00.23 (first epoch)
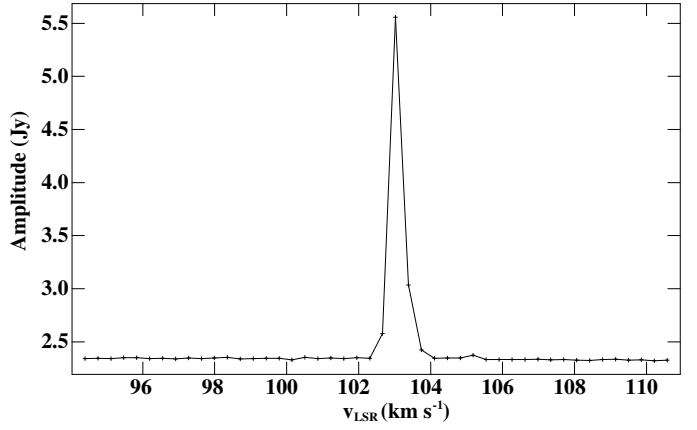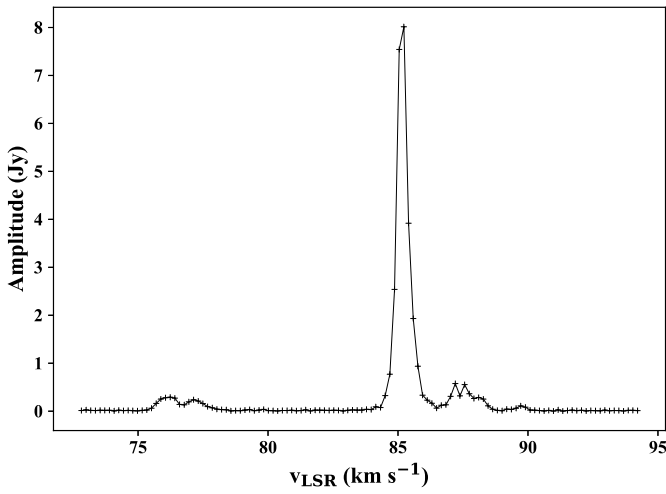

(i) 6.7 GHz methanol maser − G030.70−00.06 (second epoch)
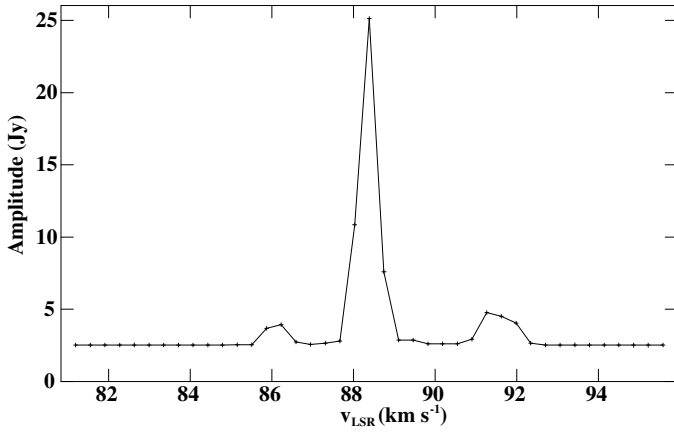
(j) 6.7 GHz methanol maser − G030.74−00.04 (second epoch)
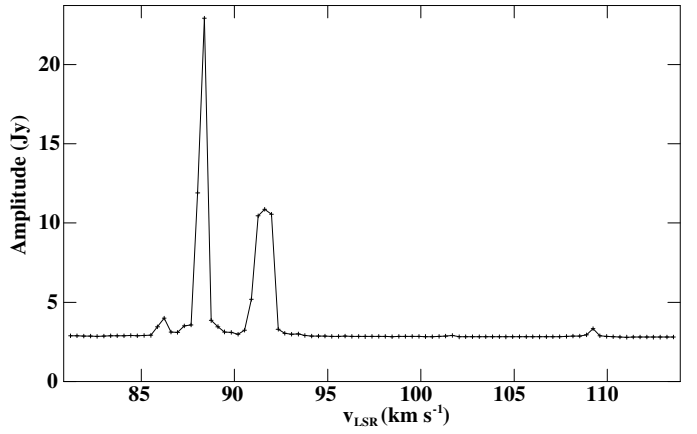
(k) 6.7 GHz methanol maser − G030.78+00.20 (second epoch)

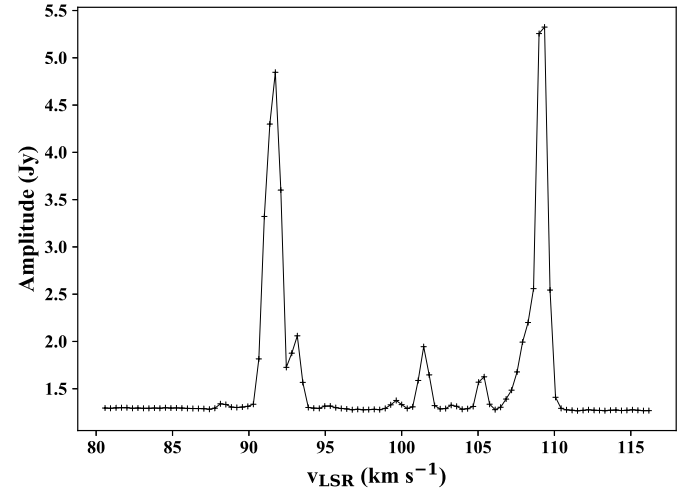(l) 6.7 GHz methanol maser − G030.81−00.05 (second epoch)
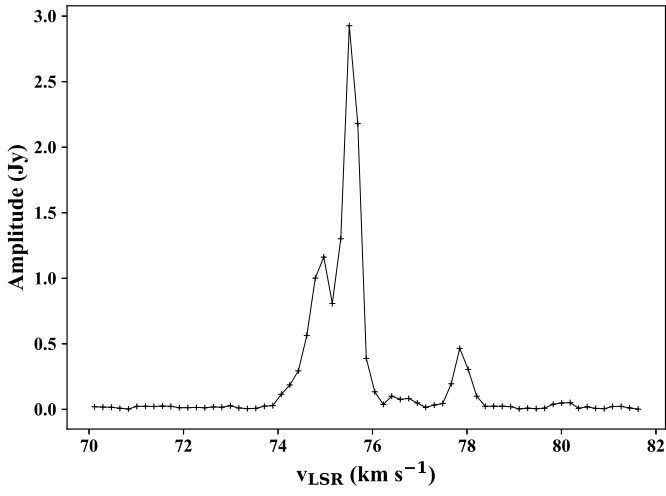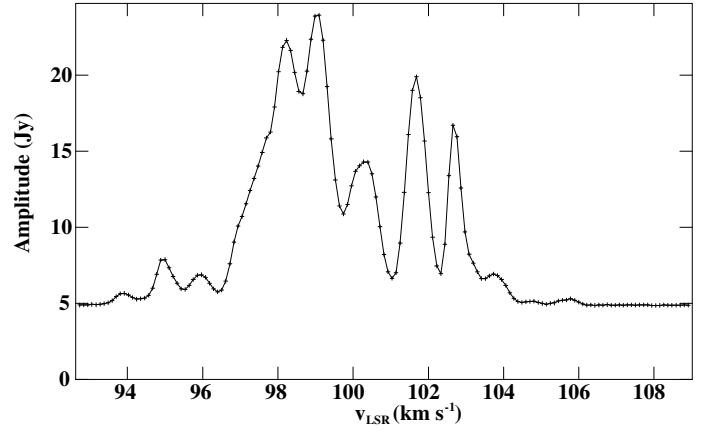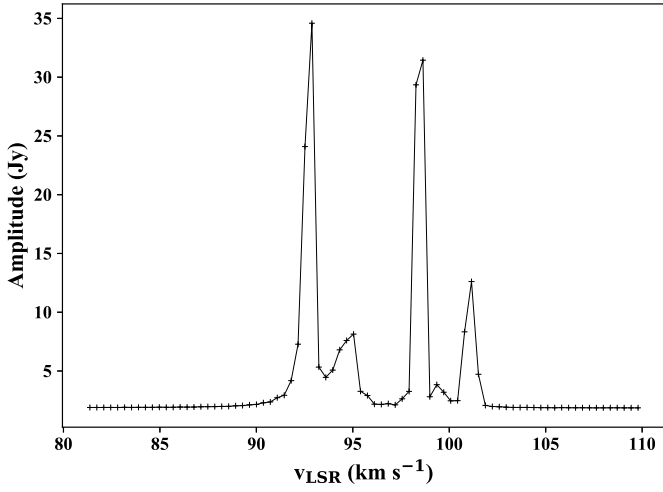
Fig. B.1: Continued.

(m) 6.7 GHz methanol maser − G030.97−00.14 (second epoch)

(n) 22 GHz water maser − G031.41+00.30 (second epoch)

(o) 6.7 GHz methanol maser − G032.04+00.05 (second epoch)

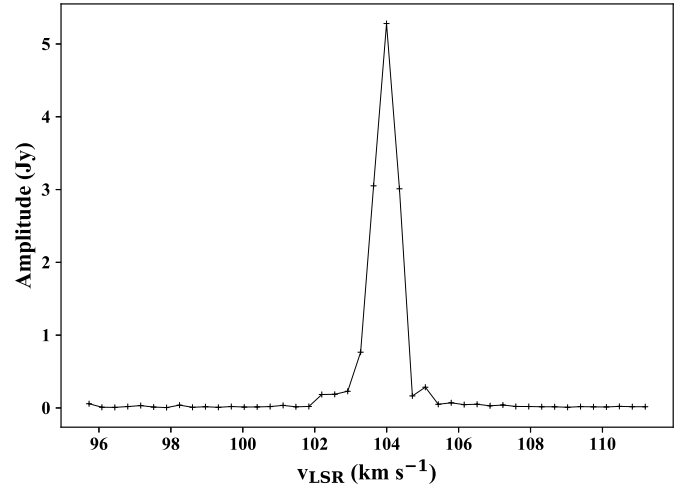(p) 6.7 GHz methanol maser − G033.09−00.07 (second epoch)

Fig. C.1: Parallax and proper motion data and fits for our 6.7 GHz methanol and 22 GHz water masers. The black symbols show the average of all quasar positions for 6.7 GHz masers. In each panel, the data of different maser spots are offset for clarity. First panel: Measured position of the maser on the sky. The positions expected from the fit are shown as open circles. Second panel: East (upper part, solid lines) and north (lower part, dashed lines) position offsets vs. time. Third panel: As second panel, but with proper motion removed, showing only the parallax effect for the maser underlined in the legend.

(a) 6.7 GHz methanol maser − G028.14−00.00

(b) 6.7 GHz methanol maser − G029.86−00.04

Fig. C.1: Continued.

(c) 6.7 GHz methanol maser − G029.95−00.01

(d) 22 GHz water maser − G029.98+00.10
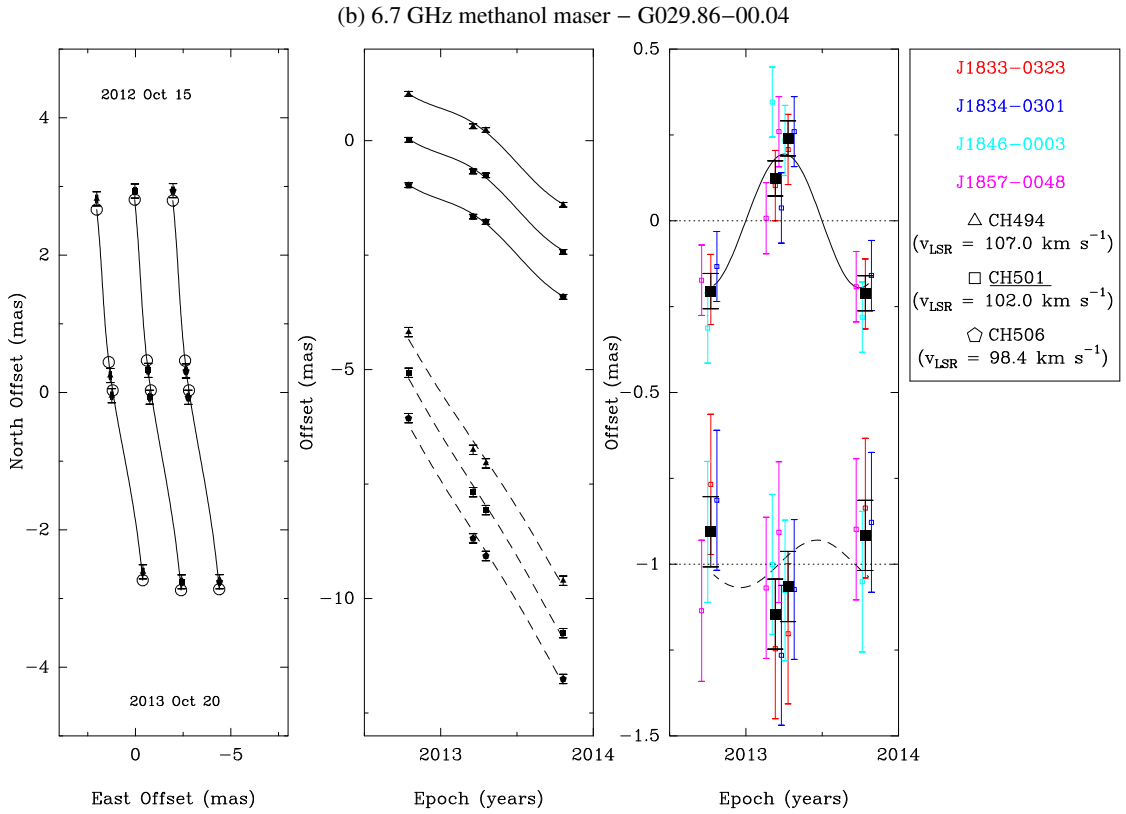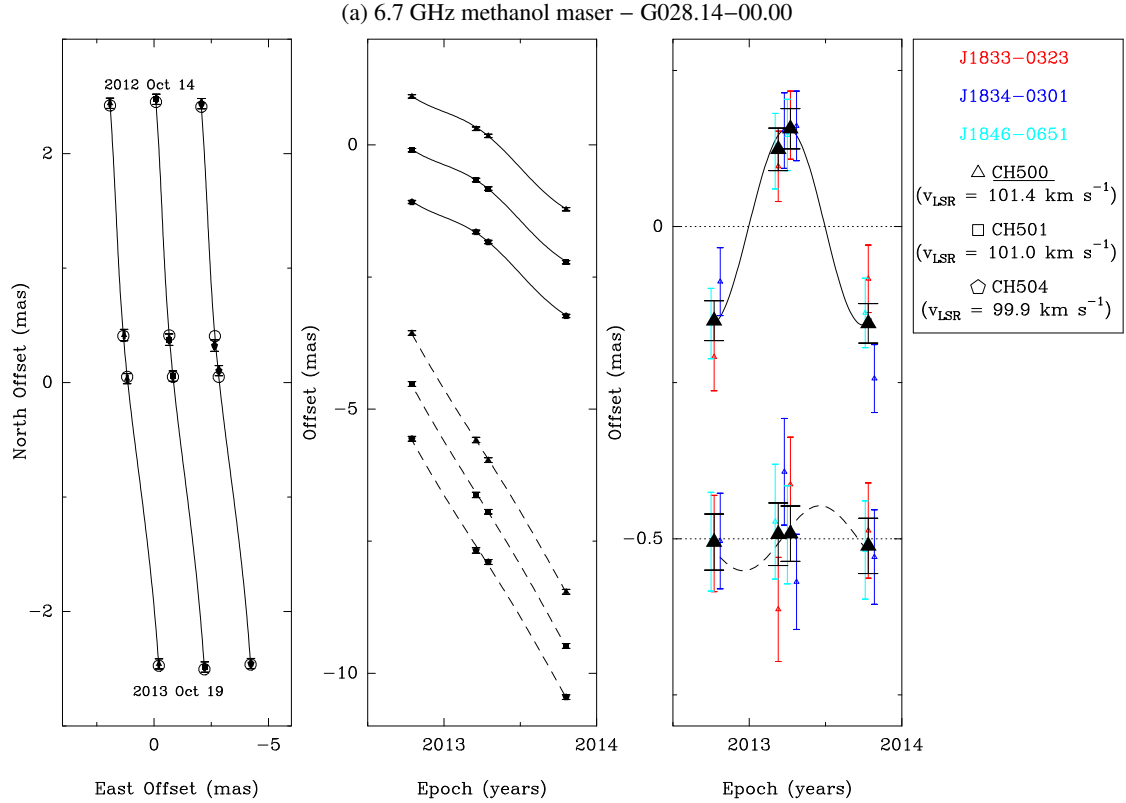
Fig. C.1: Continued.

(e) 6.7 GHz methanol maser − G030.22−00.18
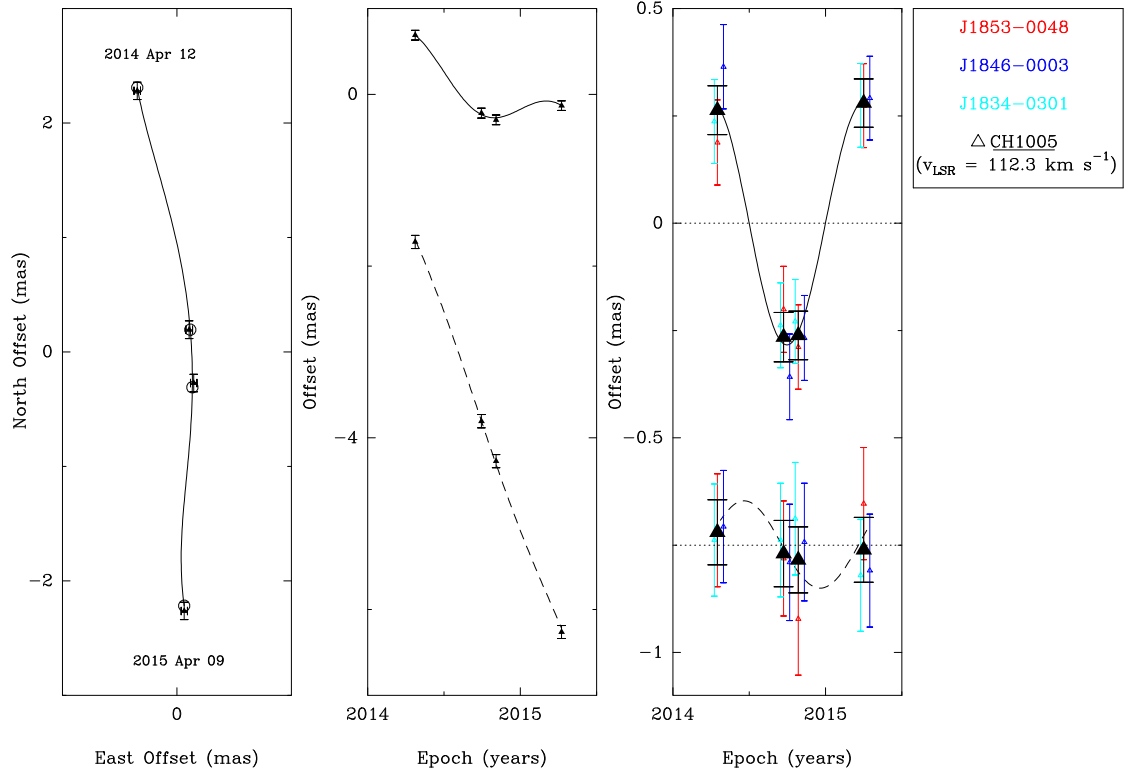
(f) 6.7 GHz methanol maser − G030.41−00.23
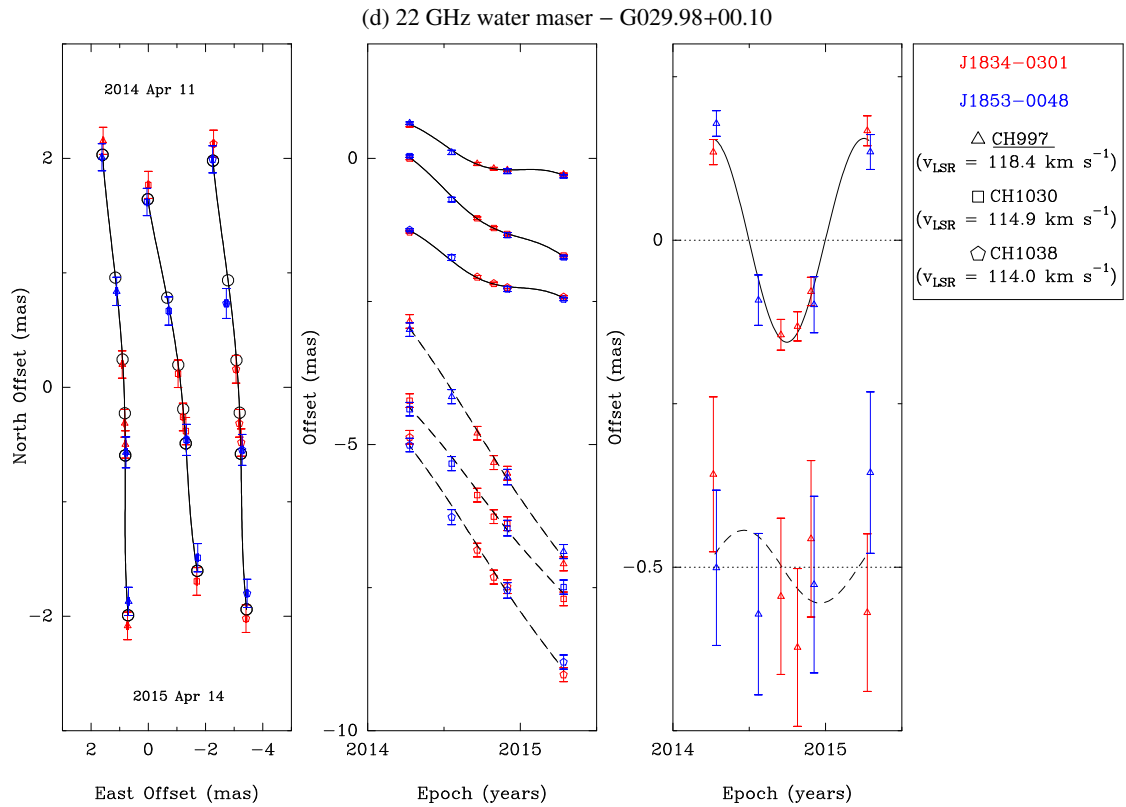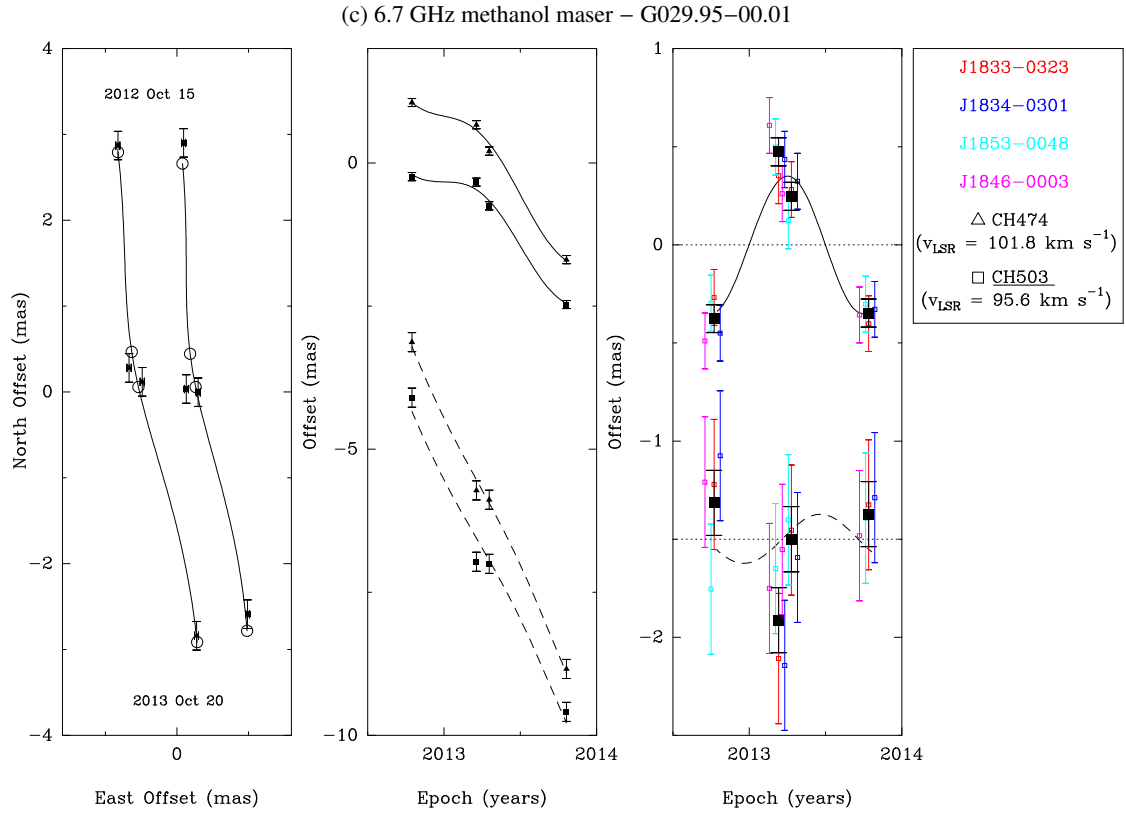
Fig. C.1: Continued.

(g) 6.7 GHz methanol maser − G030.70−00.06
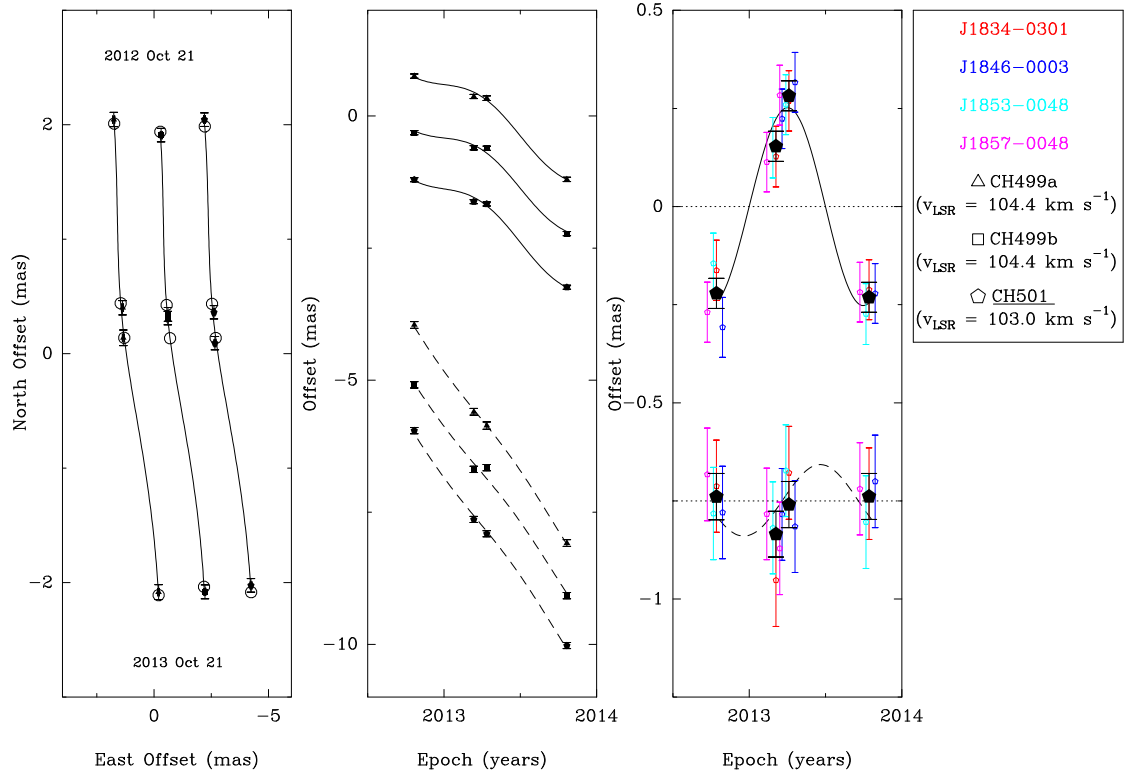
(h) 6.7 GHz methanol maser − G030.74−00.04
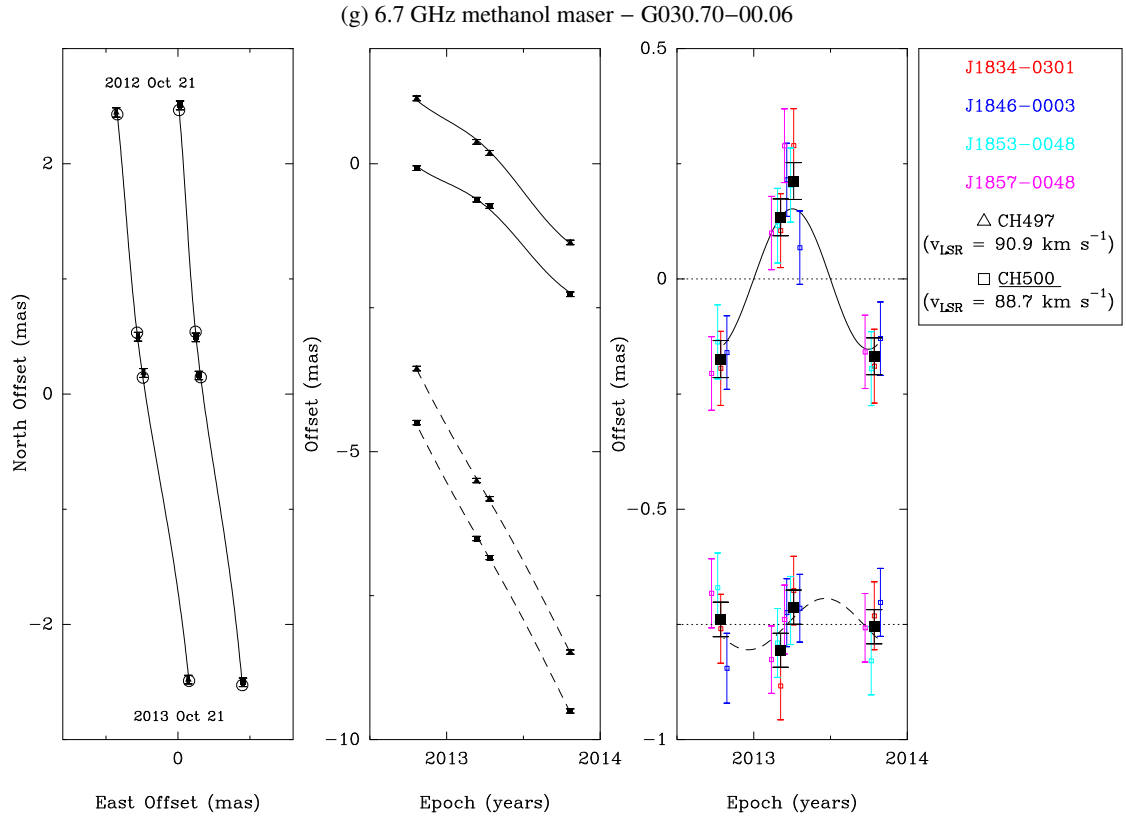
Fig. C.1: Continued.

(i) 6.7 GHz methanol maser − G030.78+00.20
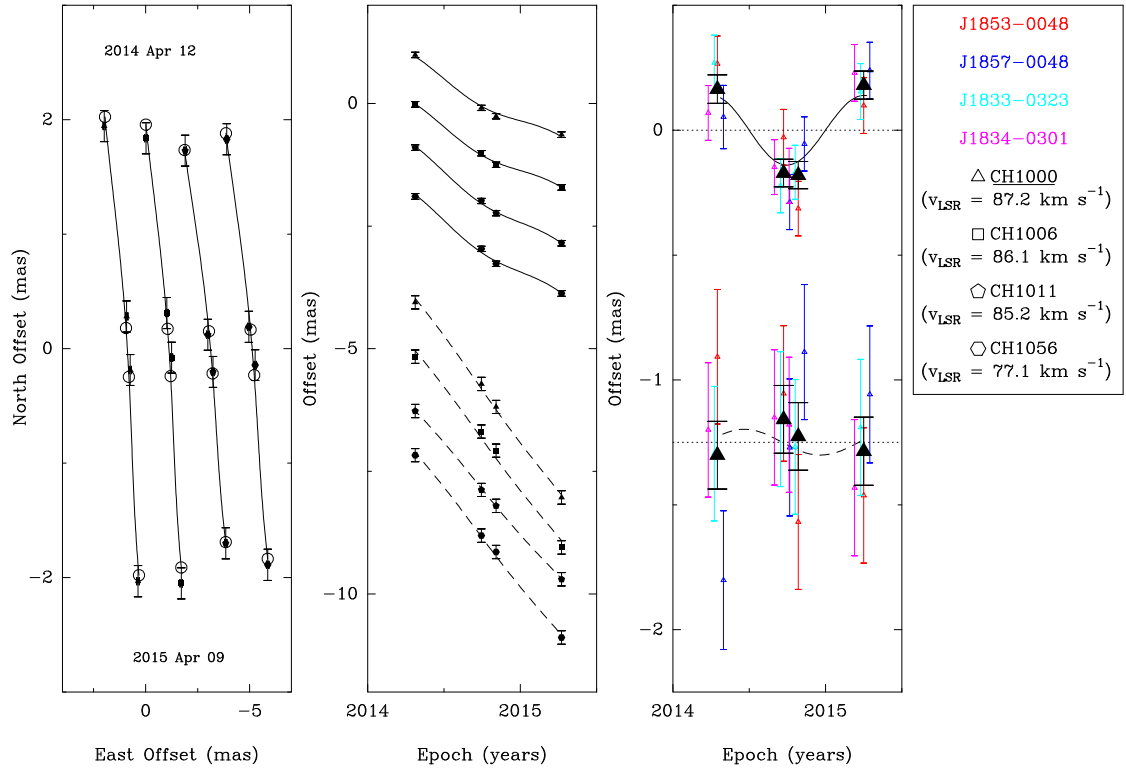
J1853−0048
J1857−0048
J1833−0323
J1834−0301
△ CH1000
(v_LSR = 87.2 km s^-1)
□ CH1006
(v_LSR = 86.1 km s^-1)
⬠ CH1011
(v_LSR = 85.2 km s^-1)
⬡ CH1056
(v_LSR = 77.1 km s^-1)

(j) 6.7 GHz methanol maser − G030.81−00.05

J1834−0301
J1846−0003
J1853−0048
J1857−0048
△ CH500a
(v_LSR =109.4 km s^-1)
□ CH503a
(v_LSR = 108.3 km s^-1)
⬠ CH505a
(v_LSR = 107.6 km s^-1)
⬡ CH507b
(v_LSR = 106.8 km s^-1)
◯ CH511a
(v_LSR = 105.4 km s^-1)
⬡ CH545a
(v_LSR = 93.2 km s^-1)

Fig. C.1: Continued.

(k) 6.7 GHz methanol maser − G030.97−00.14

(l) 22 GHz water maser − G031.41+00.30
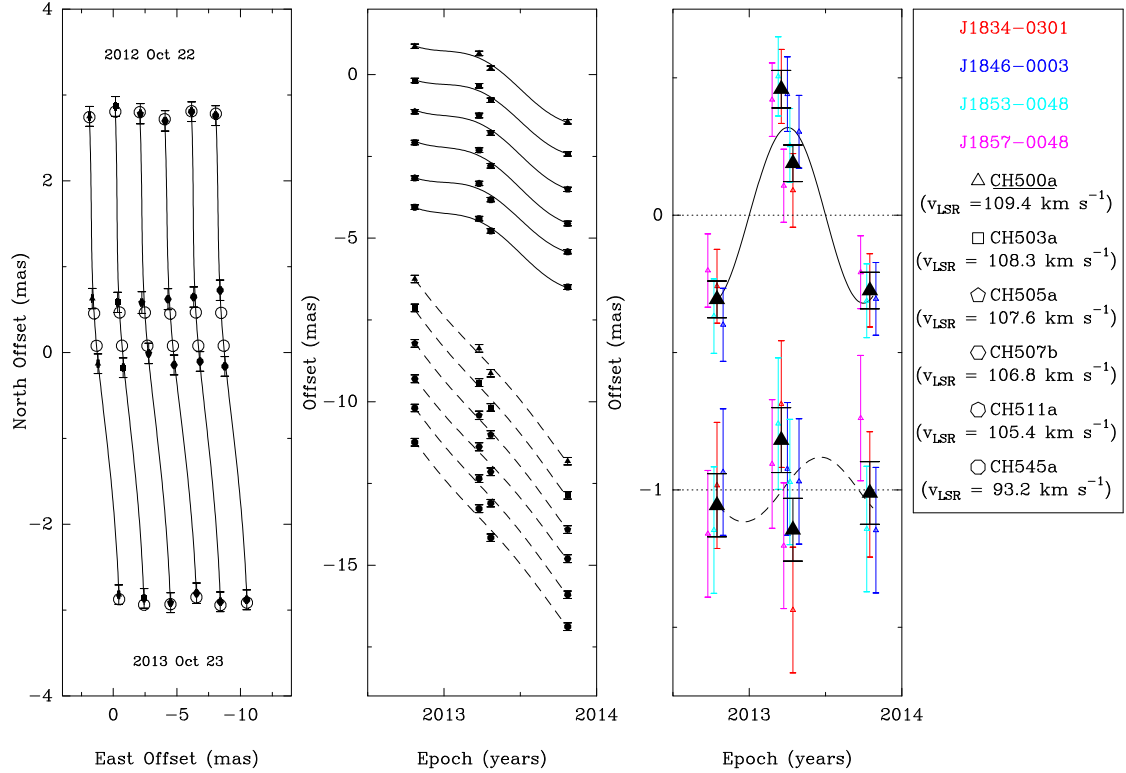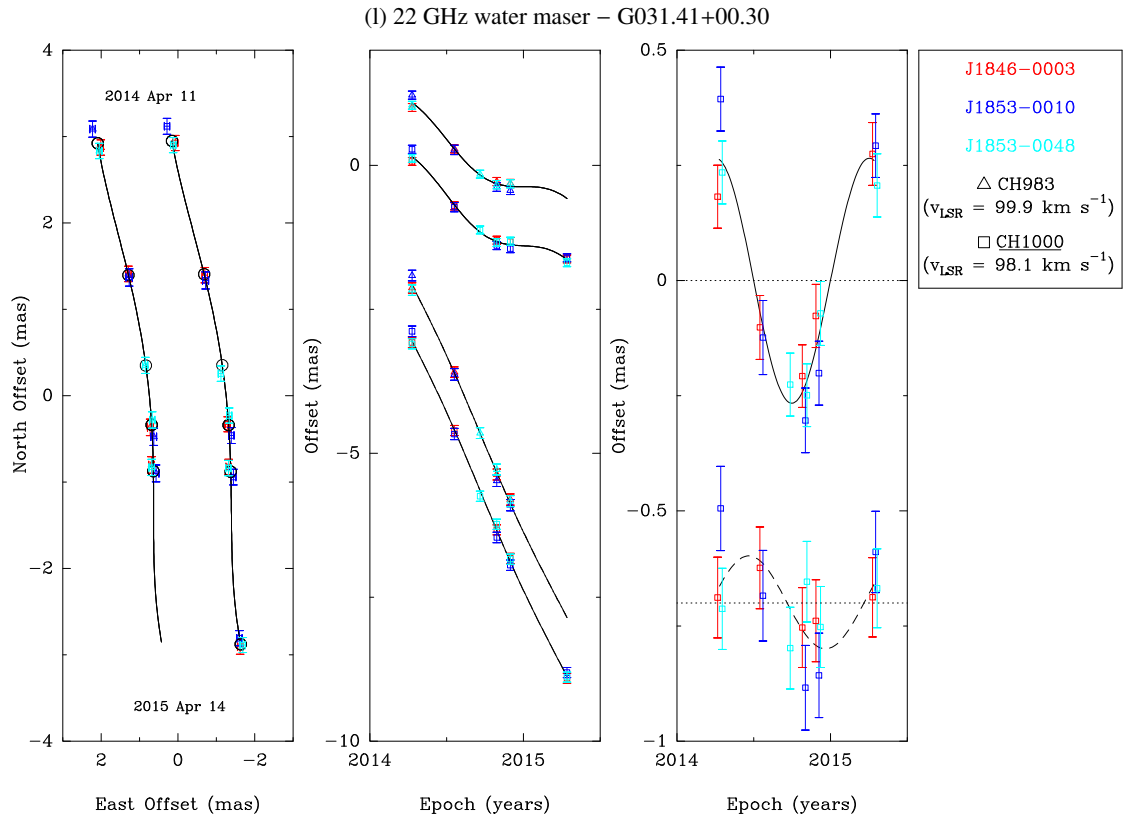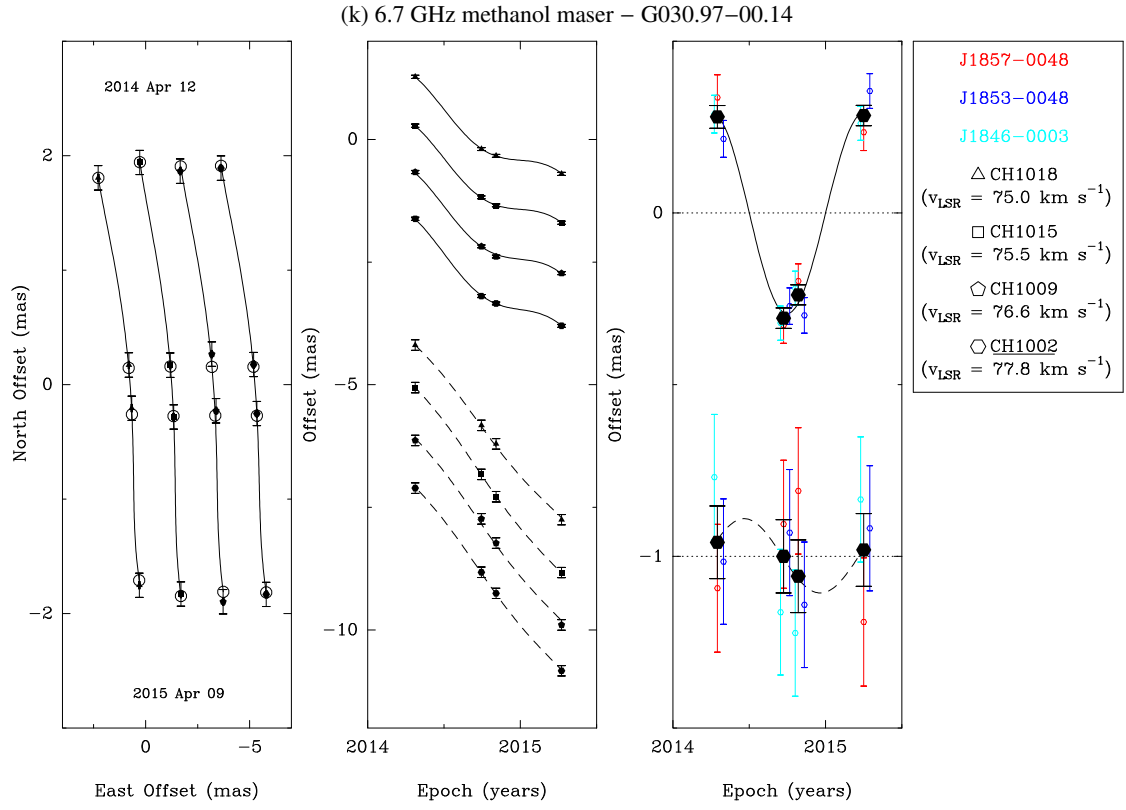
(m) 6.7 GHz methanol maser − G032.04+00.05

(n) 6.7 GHz methanol maser − G033.09−00.07
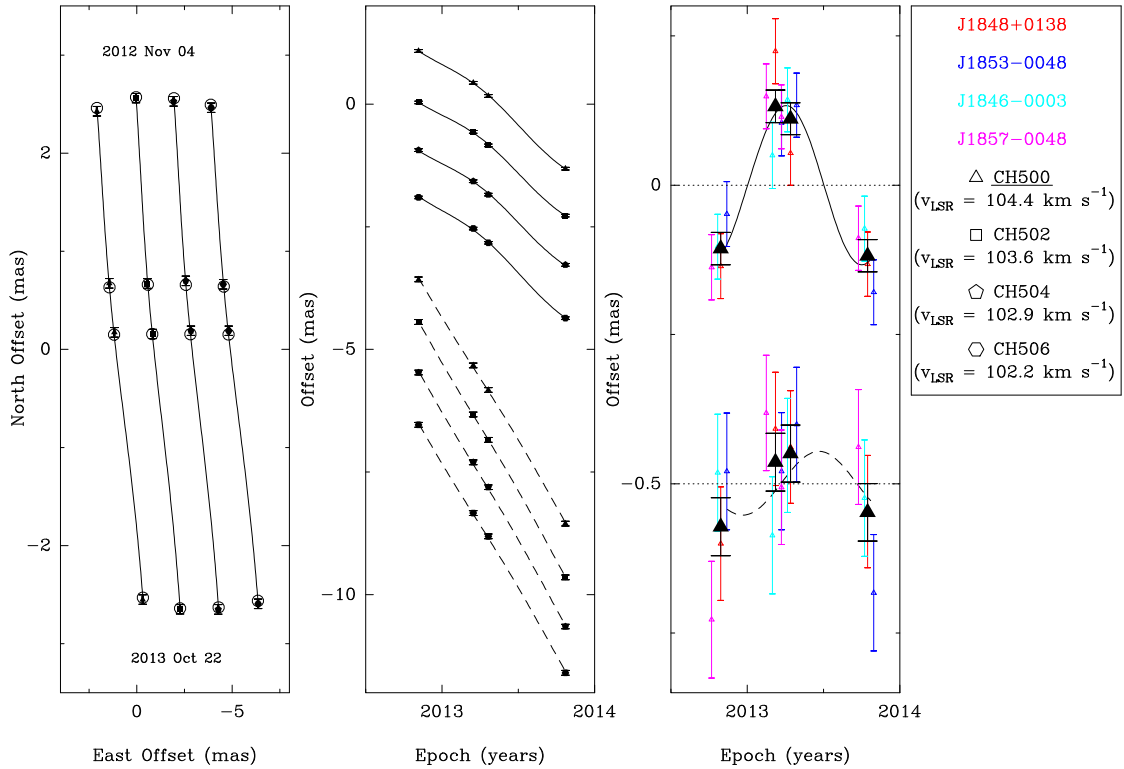
Fig. D.1: Internal motion plot. The star symbol indicates the position of the central object.

(a) 22 GHz water maser − G028.86+00.06

(b) 6.7 GHz methanol maser − G029.86−00.04

(c) 6.7 GHz methanol maser − G029.95−00.01
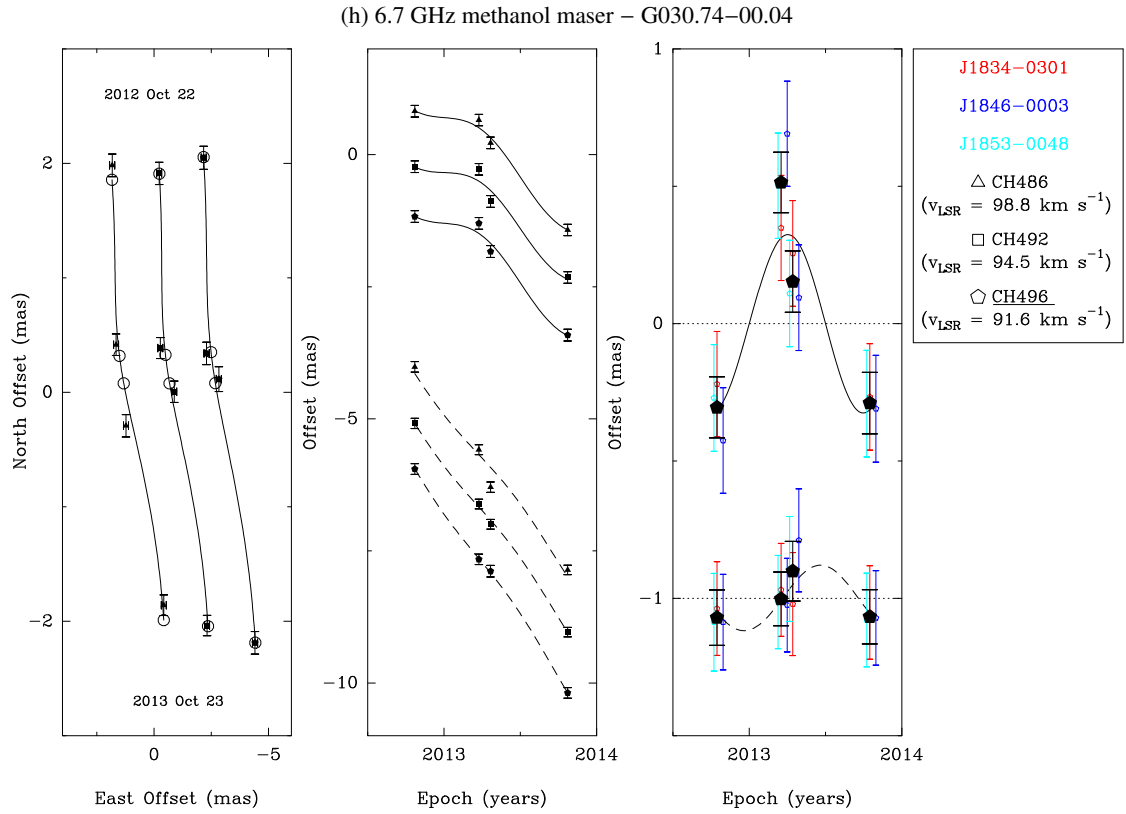
(d) 22 GHz water maser − G029.98+00.10

Fig. D.1: Continued.

(a) 6.7 GHz methanol maser − G030.41−00.23

(b) 6.7 GHz methanol maser − G030.70−00.06

(c) 6.7 GHz methanol maser − G030.74−00.04

(d) 22 GHz water maser − G031.41+00.30

Fig. E.1: Distribution of the bolometric luminosity (upper left), dust temperature (upper right), mass (lower left), and H$_2$ column density (lower right) of the host clouds of the high peculiar motion (red) and low peculiar motion (blue) sources (for sources with velocity uncertainty $\leq$ 20 km s^{-1}). The values of these parameters were taken from the ATLASGAL clump catalog of Urquhart et al. (2018).

Table A.1: Observed coordinates, line-of-sight velocities, observing times, frequency of the maser transition of our targets, and the VLBA program code of the corresponding observation . The J* sources are the background quasars that were observed as phase reference sources for the corresponding target.

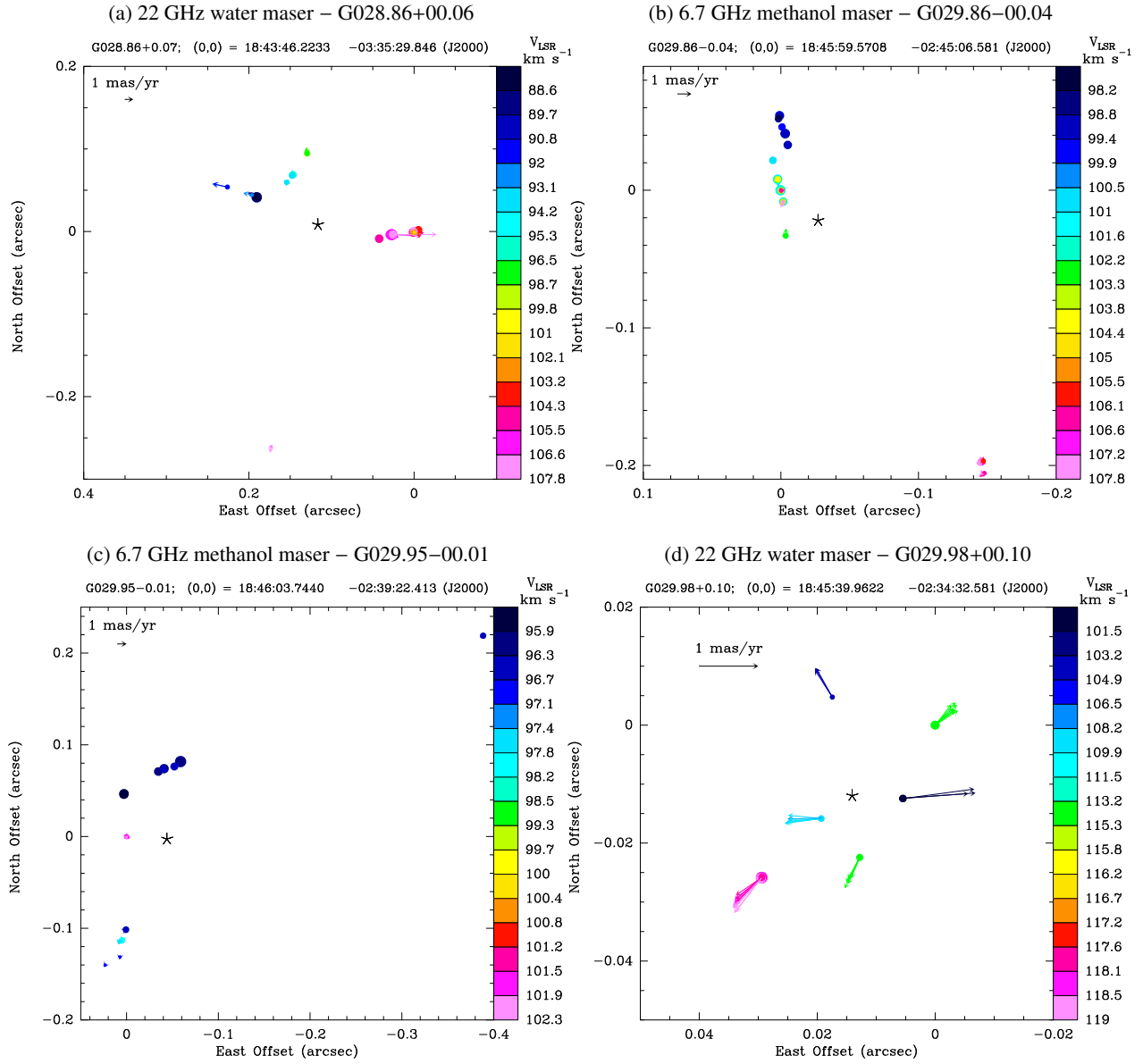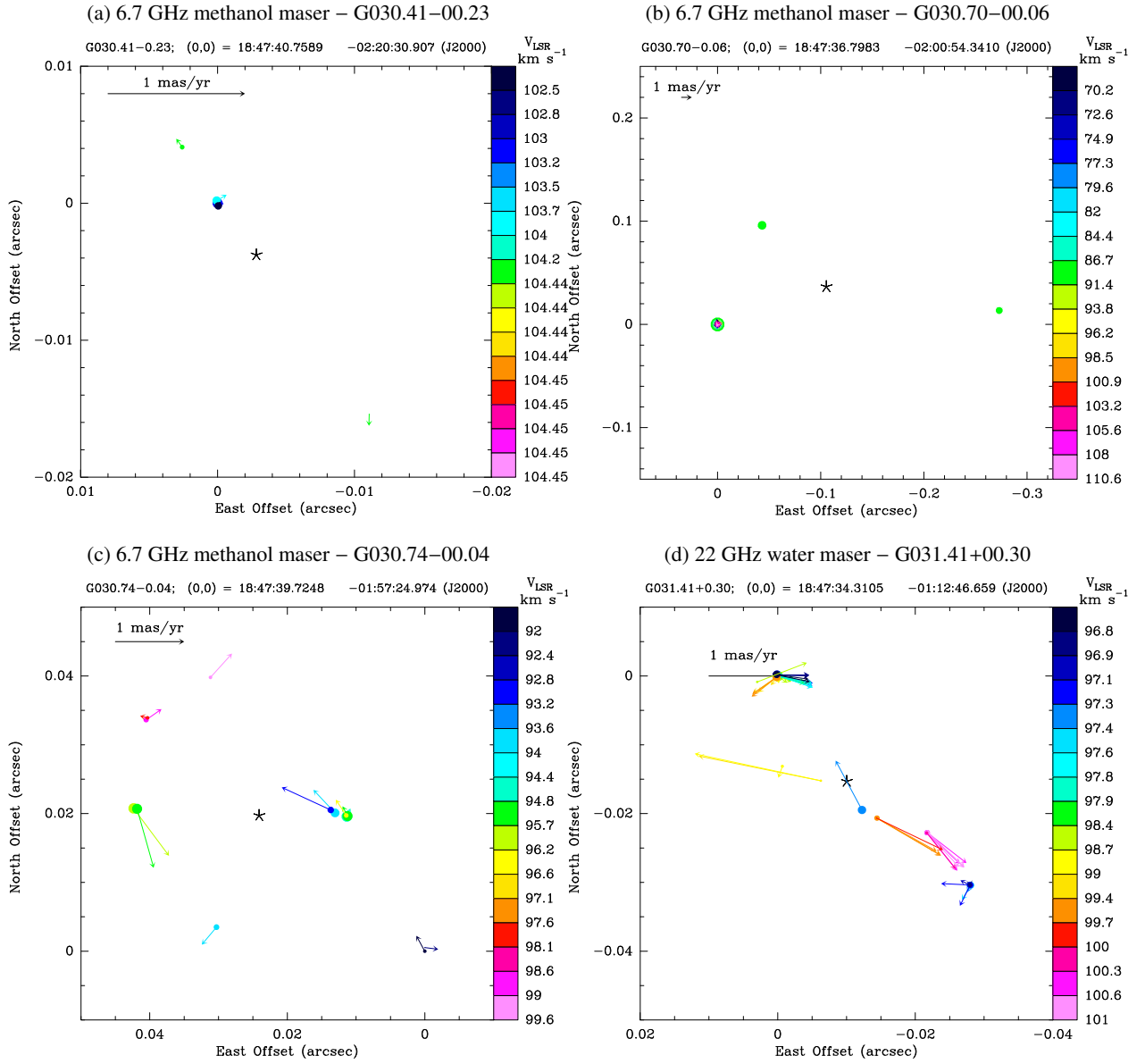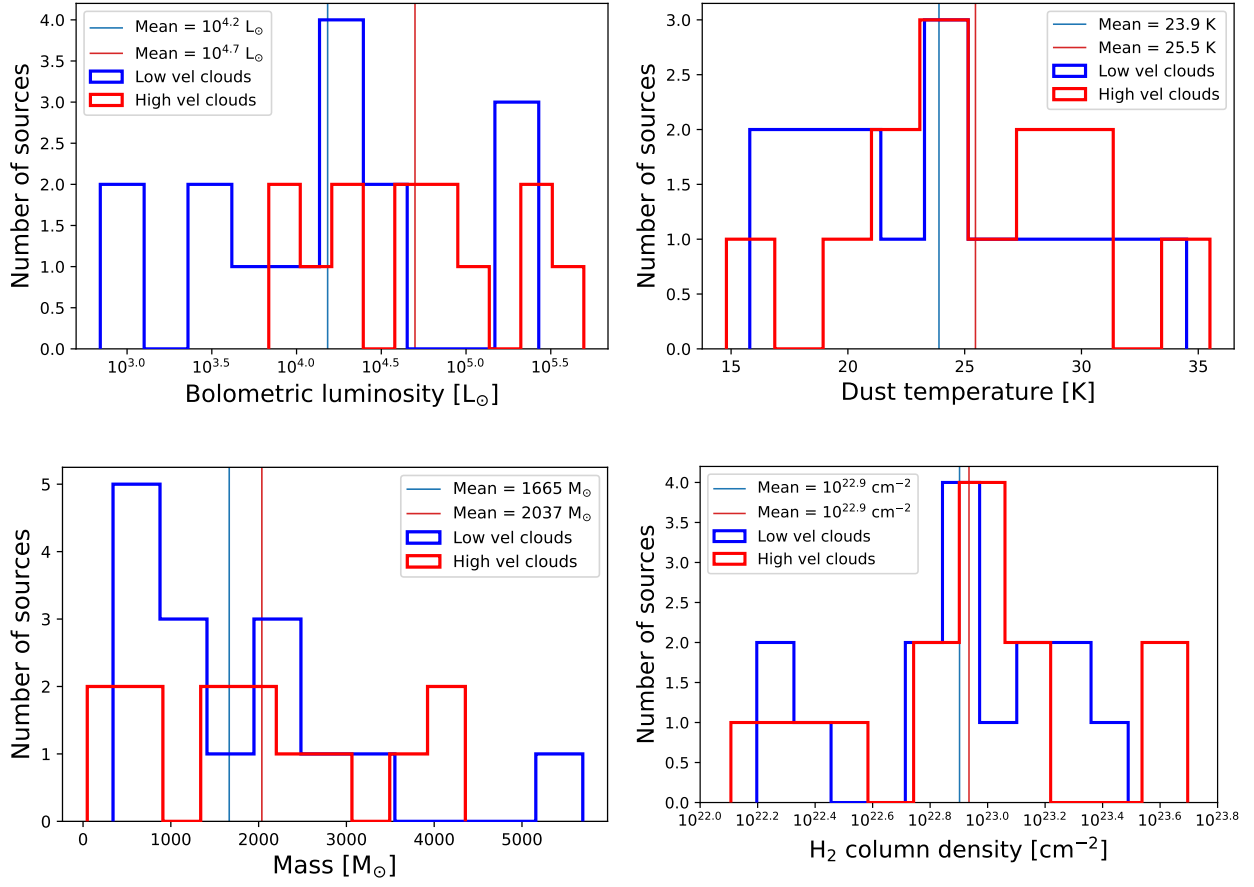| Source	RA [hh mm ss.ssss]	Dec [dd mm ss.sss]	v_{LSR} [km s^{-1}]	Observing Times	Frequency [GHz]	VLBA Program Code
G023.25−00.24	18 34 31.2392	−08 42 47.501	65	Oct 2012 − Oct 2013	6.7	BR149F
J1825−0737	18 25 37.6096	−07 37 30.013				
J1846−0651	18 46 06.3002	−06 51 27.747				
G028.14−00.00	18 42 42.5916	−04 15 35.163	101	Oct 2012 − Oct 2013	6.7	BR149H
J1833−0323	18 33 23.9055	−03 23 31.466				
J1834−0301	18 34 14.0746	−03 01 19.627				
J1827−0405	18 27 45.0404	−04 05 44.580				
J1846−0651	18 46 06.3002	−06 51 27.747				
G028.86+00.06	18 43 46.2259	−03 35 29.563	106	Feb 2011 − Apr 2012	22	BR145J
J1833−0323	18 33 23.9055	−03 23 31.466				
J1846−0651	18 46 06.3003	−06 51 27.746				
J1857−0048	18 57 51.3586	−00 48 21.950				
G029.86−00.04	18 45 59.5734	−02 45 05.528	102	Oct 2012 − Oct 2013	6.7	BR149I
J1834−0301	18 34 14.0746	−03 01 19.627				
J1833−0323	18 33 23.9055	−03 23 31.466				
J1857−0048	18 57 51.3586	−00 48 21.950				
J1846−0003	18 46 03.7826	−00 03 38.283				
G029.95−00.01	18 46 03.7431	−02 39 20.999	96	Oct 2012 − Oct 2013	6.7	BR149I
J1834−0301	18 34 14.0746	−03 01 19.627				
J1853−0048	18 53 41.9892	−00 48 54.331				
J1833−0323	18 33 23.9055	−03 23 31.466				
J1846−0003	18 46 03.7826	−00 03 38.283				
G029.98+00.10	18 45 39.9637	−02 34 32.624	118	Nov 2013 − Apr 2015	22	BR198N
J1834−0301	18 34 14.0746	−03 01 19.627				
J1853−0048	18 53 41.9892	−00 48 54.330				
J1846−0003	18 46 03.7850	−00 03 38.280				
J1857−0048	18 57 51.3586	−00 48 21.950				
G030.22−00.18	18 47 08.2900	−02 29 29.400	113	Apr 2014 − Apr 2015	6.7	BR198M
J1853−0048	18 53 41.9892	−00 48 54.330				
J1857−0048	18 57 51.3586	−00 48 21.950				
J1846−0003	18 46 03.7850	−00 03 38.280				
J1834−0301	18 34 14.0746	−03 01 19.627				
G030.41−00.23	18 47 40.7610	−02 20 30.254	103	Oct 2012 − Oct 2013	6.7	BR149J
J1853−0048	18 53 41.9892	−00 48 54.331				
J1834−0301	18 34 14.0746	−03 01 19.627				
J1857−0048	18 57 51.3586	−00 48 21.950				
J1846−0003	18 46 03.7826	−00 03 38.283				
G030.70−00.06	18 47 36.8036	−02 00 55.021	88	Oct 2012 − Oct 2013	6.7	BR149J
J1853−0048	18 53 41.9892	−00 48 54.331				
J1834−0301	18 34 14.0746	−03 01 19.627				
J1857−0048	18 57 51.3586	−00 48 21.950				
J1846−0003	18 46 03.7826	−00 03 38.283				
G030.74−00.04	18 47 37.7289	−01 57 54.699	88	Oct 2012 − Oct 2013	6.7	BR149K
J1853−0048	18 53 41.9892	−00 48 54.331				
J1834−0301	18 34 14.0746	−03 01 19.627				
J1857−0048	18 57 51.3586	−00 48 21.950				
J1846−0003	18 46 03.7826	−00 03 38.283				

Source	RA [hh mm ss.ssss]	Dec [dd mm ss.sss]	v_{LSR} [km s^{-1}]	Observing Times	Frequency [GHz]	VLBA Program Code
G030.78+00.20	18 46 48.0800	−01 48 54.000	87	Apr 2014 − Apr 2015	6.7	BR198M
J1853−0048	18 53 41.9892	−00 48 54.330				
J1857−0048	18 57 51.3586	−00 48 21.950				
J1833−0323	18 33 23.9055	−03 23 31.466				
J1834−0301	18 34 14.0746	−03 01 19.627				
G030.81−00.05	18 47 46.9764	−01 54 26.676	109	Oct 2012 − Oct 2013	6.7	BR149K
J1853−0048	18 53 41.9892	−00 48 54.331				
J1834−0301	18 34 14.0746	−03 01 19.627				
J1857−0048	18 57 51.3586	−00 48 21.950				
J1846−0003	18 46 03.7826	−00 03 38.283				
G030.97−00.14	18 48 22.0300	−01 48 30.600	78	Apr 2014 − Apr 2015	6.7	BR198M
J1857−0048	18 57 51.3586	−00 48 21.950				
J1853−0048	18 53 41.9892	−00 48 54.330				
J1846−0003	18 46 03.7850	−00 03 38.280				
G031.41+00.30	18 47 34.3124	−01 12 47.000	98	Nov 2013 − Apr 2015	22	BR198N
J1853−0048	18 53 41.9892	−00 48 54.330				
J1846−0003	18 46 03.7850	−00 03 38.280				
J1853−0010	18 53 10.2692	−00 10 50.740				
J1857−0048	18 57 51.3586	−00 48 21.950				
G032.04+00.05	18 49 36.5732	−00 45 42.650	99	Nov 2012 − Oct 2013	6.7	BR149L
J1853−0048	18 53 41.9892	−00 48 54.331				
J1857−0048	18 57 51.3586	−00 48 21.950				
J1846−0003	18 46 03.7826	−00 03 38.283				
J1848+0138	18 48 21.8104	+01 38 26.632				
G033.09−00.07	18 51 59.4085	+00 06 34.262	104	Nov 2012 − Oct 2013	6.7	BR149L
J1853−0048	18 53 41.9892	−00 48 54.331				
J1857−0048	18 57 51.3586	−00 48 21.950				
J1846−0003	18 46 03.7826	−00 03 38.283				
J1848+0138	18 48 21.8104	+01 38 26.632				

Table C.1: Velocity range of the maser emission, phase reference sources, and maser channels used for parallax fitting.

Source	v_{Maser} [km s^{-1}]	Phase reference sources	Maser channels	Figs.
G023.25−00.24	55−70	J1825−0737	500	B.1a, 1a
		J1846−0651	501	
			502	
			503a	
			503b	
			514	
G028.14−00.00	98−105	J1833−0323	500	B.1b, C.1a
		J1834−0301	501	
		J1846−0651	504	
G028.86+00.06	85−110	J1833−0323	126	B.1c, 1b, D.1a
		J1857−0048	136	
		J1846−0651	155	
			171	
G029.86−00.04	95−107	J1833−0323	494	B.1d, C.1b, D.1b
		J1857−0048	501	
		J1846−0003	506	
		J1834−0301		
G029.95−00.01	93−108	J1833−0323	474	B.1e, C.1c, D.1c
		J1853−0048	503	
		J1846−0003		
		J1834−0301		
G029.98+00.10	98−120	J1834−0301	997	B.1f, C.1d, D.1d
		J1853−0048	1030	
			1038	
G030.22−00.18	110−115	J1834−0301	1005	B.1g, C.1e
		J1853−0048		
		J1846−0003		
G030.41−00.23	102−106	J1834−0301	499a	B.1h, C.1f, D.1a
		J1853−0048	499b	
		J1846−0003	501	
		J1857−0048		
G030.70−00.06	85−93	J1834−0301	497	B.1i, C.1g, D.1b
		J1853−0048	500	
		J1846−0003		
		J1857−0048		
G030.74−00.04	85−110	J1834−0301	486	B.1j, C.1h, D.1c
		J1853−0048	492	
		J1846−0003	496	
G030.78+00.20	75−91	J1834−0301	1000	B.1k, C.1i
		J1853−0048	1006	
		J1833−0323	1011	
		J1857−0048	1056	
G030.81−00.05	87−112	J1834−0301	498	B.1l, C.1j
		J1853−0048	499	
		J1846−0003	500	
		J1857−0048	501	
			502	
			503	
			504	

Source	v_{Maser} [km s^{-1}]	Phase reference sources	Maser channels	Figs.
			505	
			507	
			509	
			511	
			512	
			544	
			545	
G030.97−00.14	72−81	J1846−0003	1002	B.1m, C.1k
		J1853−0048	1009	
		J1857−0048	1015	
			1018	
G031.41+00.30	93−107	J1846−0003	983	B.1n, C.1l, D.1d
		J1853−0010	1000	
		J1853−0048		
G032.04+00.05	90−103	J1848+0138	494a	B.1o, C.1m
		J1857−0048	495a	
			496a	
			499a	
			500a	
			501a	
			504	
			505	
			507	
			509	
			511	
			512	
			544	
			545	
G033.09−00.07	101−107	J1848+0138	500	B.1p, C.1n
		J1857−0048	502	
			504	
			506	